

Upper critical fields in high- T_c superconductors

Wei Wei,¹ Yuling Xiang,¹ Qiang Hou,¹ Yue Sun,^{1,*} Zhixiang Shi^{1,†}

¹*Department of Physics, Southeast University, Nanjing 211189, China*

Since the discovery of high-temperature superconductivity in cuprates, understanding the unconventional pairing mechanism has remained one of the most significant challenges. The upper critical field (H_{c2}) is an essential parameter for obtaining information on the pair-breaking mechanism, coherence length ξ , and pairing symmetry, all of which are crucial for understanding unconventional superconducting mechanisms. Here, we provide a brief review of studies on H_{c2} in several representative series of cuprate, iron-based, and nickelate superconductors. By comparing the behavior of H_{c2} as a function of temperature, doping concentration, and anisotropy across these three major classes of superconductors, we hope to contribute to a better understanding of the complex pairing interactions in high-temperature superconductors.

Keywords: high-temperature superconductivity; cuprate superconductors; iron-based superconductors; nickelate superconductors

1. Introduction

In 1986, Bednorz and Müller made the groundbreaking discovery of high-temperature superconductivity in the Ba-doped insulating cuprate system $\text{La}_{2-x}\text{Ba}_x\text{CuO}_4$ [1]. By 2008, the discovery of iron-based superconductors (FeSCs) provided new insights into the pairing mechanisms of high-temperature superconductors (HTS) and fueled the pursuit of materials with higher T_c [2, 3]. Over approximately three decades of research, cuprates and FeSCs have been recognized as the only two systems of high-temperature superconductors under ambient pressure. Ongoing discussions regarding the superconducting pairing mechanisms have led to the proposal of various superconducting pairing models that do not involve electron-phonon coupling. Until 2019, Li *et al.* discovered superconductivity in Sr-doped NdNiO_2 at temperatures between 9 and 15 K [4]. More recently, in 2023, Wang *et al.* identified signatures of superconductivity near 80 K in $\text{La}_3\text{Ni}_2\text{O}_7$ under high pressure, suggesting that nickelate superconductors may represent a new class of high-temperature superconductors [5]. These findings provide a new platform to explore the mechanisms of high-temperature superconductivity, further stimulating research into the pairing mechanisms underlying high-temperature superconductivity.

Upper critical field, H_{c2} , is a fundamental parameter for getting information such as the pair-breaking mechanism, coherence length ξ , anisotropy, and pairing symmetry — all of which play important roles in understanding unconventional superconductivity [6–8]. In type-II superconductors, the origins of H_{c2} are classified as two distinct pair-breaking mechanisms. One is the orbital pair-breaking effect, where the Lorentz force acts on Cooper pairs with opposite momenta, and the superconductivity is destroyed when the kinetic energy exceeds the con-

densation energy of the Cooper pairs. The other is the spin-paramagnetic pair-breaking effect, which arises from the Zeeman splitting of spin-singlet cooper pairs. In this case, superconductivity is suppressed when the Pauli spin magnetization exceeds the condensation energy as the critical magnetic field is reached. The analysis and comparison of H_{c2} behaviors in the three major classes of unconventional superconductors—cuprates, FeSCs, and nickelates—are crucial for understanding the mechanisms behind unconventional pairing.

To begin with, it is essential to compare the physical properties among these three types of unconventional HTS. The major comparisons can be summarized as follows: (i) All these superconductors are layered compounds, with crystal structures containing CuO , FeAs/FeSe , or NiO layers. Various atoms or molecules can be intercalated between these layers, altering the lattice constants or even modifying the crystal structures, which leads to the formation of various superconducting phases. (ii) The parent compounds of cuprates and infinite-layer nickelates are Mott insulators [9, 10], with superconductivity emerging upon chemical doping. In contrast, the parent compounds of FeSCs are antiferromagnetism [11]. (iii) In terms of electronic structure, x-ray absorption spectroscopy and resonant inelastic x-ray scattering have shown that LaNiO_2 and NdNiO_2 have a nominal $3d^9$ electronic configuration, analogous to the Cu^{2+} state in cuprates [12]. However, the Fe^{2+} electronic configuration in iron-based superconductors is different, with two unpaired electrons [13]. (iv) Regarding band structure, most cuprates exhibit a single-band characteristic, with intraorbital interactions as the sole driving force for pairing, resulting in a d -wave gap [14]. Only a few cuprate superconductors, such as $\text{Nd}_{2-x}\text{Ce}_x\text{CuO}_{4+\delta}$, exhibit multi-band characteristics. In contrast, most FeSC and infinite-layer nickelate superconductors are multiband systems, requiring both intraorbital and interorbital interactions for pairing [15, 16].

In this review, we first provide a brief introduction to

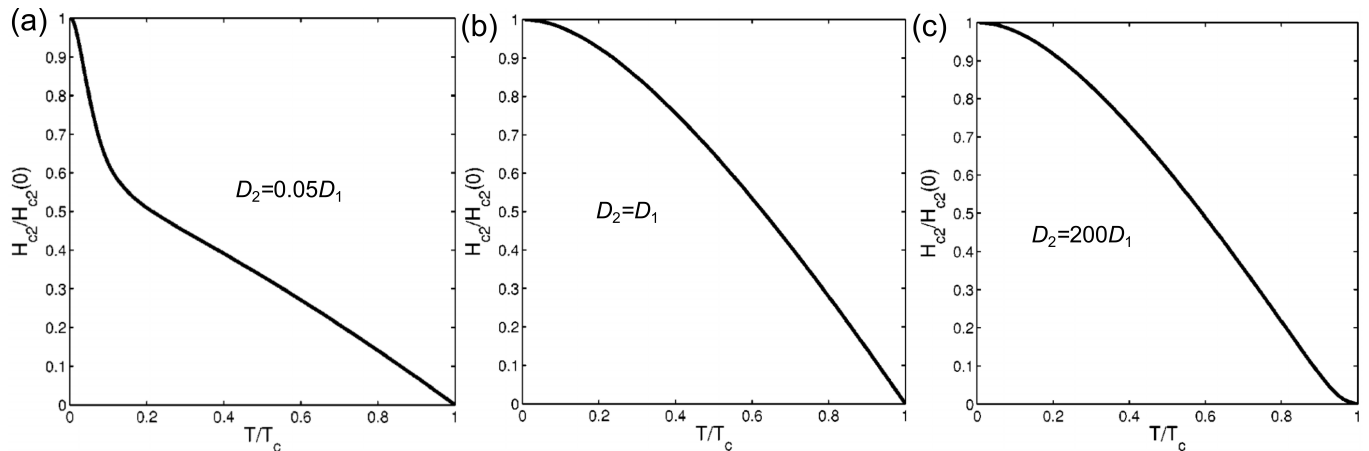


FIG. 1. (a) Temperature dependence of $H_{c2}(T)$, calculated from Eq. (10) for various ratios of D_2/D_1 [17], was determined for MgB₂ [18]. σ and π represent different orbitals.

the theoretical models of H_{c2} in Section 2. Subsequently, in Sections 3 to 5, we offer an overview of the temperature and doping dependence, as well as the anisotropy, of H_{c2} in cuprate, iron-based, and nickelate superconductors. Finally, we conclude the review with a summary and outlook in Section 6.

2. Theoretical models of H_{c2}

2.1. Ginzburg-Landau (GL) model

The Ginzburg-Landau (GL) theory provides a phenomenological framework for understanding superconductivity near T_c . Specifically, within the context of H_{c2} , the GL theory primarily focuses on orbital effects, which arise from the interaction between Cooper pairs and an applied magnetic field due to their orbital motion. Within this framework, the behavior of H_{c2} is closely related to the coherence length ξ and the penetration depth λ , which characterize the spatial variation of the superconducting order parameter and the magnetic field, respectively.

$$H_{c2}^{\text{GL}}(T) = \frac{\Phi_0}{2\pi\xi_{ab}^2(T)}, \quad (1)$$

where Φ_0 denotes the magnetic flux quantum. In a general scenario, an anisotropic superconductor is characterized by direction-dependent H_{c2} and two distinct coherence lengths, depending on the orientation of the magnetic field along different high-symmetry axes. First, when the magnetic field is oriented parallel to the crystallographic c axis ($H \parallel c$), the GL coherence length of Cooper pairs forming screening orbits in the ab -plane can

be expressed as [19]

$$\xi_{ab}^{\text{GL}} = \sqrt{\frac{\Phi_0}{2\pi T_c \mu_0 \left| \frac{dH_{c2}^c}{dT} \right|_{T_c}}}. \quad (2)$$

Here, $\mu_0 \frac{dH_{c2}^c}{dT}$ is the slope of H_{c2}^c ($H \parallel c$) in the limit of T near T_c . For the case where the magnetic field is oriented along the ab -plane ($H \parallel ab$), the coherence length along the c axis can be expressed as:

$$\xi_c^{\text{GL}} = \frac{\Phi_0}{2\pi T_c \mu_0 \left| \frac{dH_{c2}^{ab}}{dT} \right|_{T_c} \xi_{ab}^{\text{GL}}}. \quad (3)$$

In this scenario, $\mu_0 \left| \frac{dH_{c2}^{ab}}{dT} \right|_{T_c}$ is the slope of H_{c2}^{ab} near T_c . One issue within the GL model for anisotropic superconductors is the assumption of a linear temperature dependence of H_{c2} . At low temperatures, this assumption often leads to an overestimation of H_{c2} , resulting in an underestimation of the coherence lengths. To more accurately determine the coherence lengths, measurements of H_{c2} at low temperatures are essential. When measured at $T \rightarrow 0$ the equations can be modified as follows:

$$\xi_{ab}^{\text{GL}} = \sqrt{\frac{\Phi_0}{2\pi\mu_0 H_{c2}^c(T \rightarrow 0)}} \quad (4)$$

and

$$\xi_c^{\text{GL}} = \frac{\Phi_0}{2\pi\mu_0 H_{c2}^{ab}(T \rightarrow 0) \xi_{ab}^{\text{GL}}}. \quad (5)$$

Here, ξ_{ab} and ξ_c are the true coherence lengths at zero temperature, with $H_{c2}^c(T \rightarrow 0)$ representing the upper critical field as the temperature approaches zero. However, this approach does not account for factors like Pauli paramagnetism, which may alter the upper critical field.

2.2. Single-band WHH model

In 1966, Werthamer, Helfand, and Hohenberg developed a comprehensive model that accounts for the orbital effect, Pauli paramagnetism, and spin-orbit scattering, known as the WHH model for H_{c2} . This theory is applicable to single-band superconductors in the dirty limit ($l \ll \xi$). By incorporating the Maki parameter α_M , representing the relative strength of orbital and spin pair-breaking, and λ_{so} , representing spin-orbit scattering, the relationship between temperature and H_{c2} can be expressed using the double gamma function [20]:

$$\ln\left(\frac{1}{t}\right) = \left(\frac{1}{2} + \frac{i\lambda_{so}}{4\gamma}\right)\psi\left(\frac{1}{2} + \frac{\bar{h} + \frac{1}{2}\lambda_{so} + i\gamma}{2t}\right) + \left(\frac{1}{2} - \frac{i\lambda_{so}}{4\gamma}\right)\psi\left(\frac{1}{2} + \frac{\bar{h} + \frac{1}{2}\lambda_{so} - i\gamma}{2t}\right) - \psi\left(\frac{1}{2}\right). \quad (6)$$

Here, $t = T/T_c$ denotes the reduced temperature, ψ is the digamma function, and $\gamma = [(\alpha_M \bar{h})^2 - (\lambda_{so}/2)^2]$. The reduced magnetic field \bar{h} is defined as $\bar{h} = (4/\pi^2)H_{c2}/| -dH_{c2}/dt|_{t=1}$, where $dH_{c2}/dt|_{t=1}$ represents the slope of H_{c2} near T_c . The above equation can be numerically solved to determine the temperature dependence of H_{c2} . By fitting the experimental $H_{c2}(T)$ data using WHH theory, the parameters λ_{so} and α_M can be extracted. In the absence of both the spin-paramagnetic effect and spin-orbit interaction, $\alpha_M = 0$ and $\lambda_{so} = 0$, the orbital-limited upper critical field is given by:

$$H_{c2}^{\text{orb}} = -0.693 \frac{dH_{c2}}{dT} \Big|_{T=T_c}. \quad (7)$$

In the clean limit, the prefactor is replaced by -0.73, meaning that

$$H_{c2}^{\text{orb,clean}} = -0.73 \frac{dH_{c2}}{dT} \Big|_{T=T_c}. \quad (8)$$

As previously discussed, there are two mechanisms for breaking Cooper pairs in the presence of a magnetic field: the orbital pair-breaking effect and the spin-paramagnetic pair-breaking effect. In the latter case, as the magnetic field exceeds the Zeeman energy, one of the spins in the Cooper pair flips, leading to pair breaking. This critical magnetic field is known as the Pauli-limiting field, and it is determined by the equation [21, 22]:

$$\frac{\chi_N(H_p)^2}{2} = \frac{N(E_F)\Delta^2}{2}, \quad (9)$$

where $\chi_N = g\mu_B^2 N(E_F)$ represents the spin susceptibility in the normal state. g is the Lande g factor, μ_B

is the Bohr magneton, Δ is the superconducting gap and $N(E_F)$ is the density of state at the Fermi level E_F . In the weak-coupling BCS limit, $2\Delta(0) = 3.53k_B T_c$, and assuming $g = 2$, the Pauli-limiting field is given by $H_p^{\text{BCS}}(0) = 1.84T_c$. When considering strong coupling corrections that include electron-boson and electron-electron interactions, the Pauli-limiting field is determined by the expression $H_p = 1.86(1 + \lambda)^\epsilon \eta_\Delta \eta_{ib}(1 - I)$. The Stoner factor I is expressed as $I = N(0)J$, where J represents an effective exchange integral. The parameter η_{ib} is introduced to describe phenomenologically the effect of gap anisotropy, multiband character, energy dependence of states etc. The relationship between the orbital limit $H_{c2}^{\text{orb}}(0)$ and the Pauli limit $H_p(0)$ is given by:

$$H_{c2}^p(0) = H_{c2}^{\text{orb}}(0)/(1 + \alpha_M^2). \quad (10)$$

2.3. Two-band model

The aforementioned WHH model applies to single-band superconductors in the dirty limit and has been successfully used to describe the behavior of $H_{c2}(T)$. However, for iron-based superconductors and other systems that exhibit multiband characteristics, the WHH model is not applicable. Instead, a two-band model in the dirty limit, which does not include paramagnetic effects or spin-orbit scattering (unlike the WHH model), has been derived in Ref. [17]:

$$a_1[\ln t + U(h)] + a_2[\ln t + U(\eta h)] + a_0[\ln t + U(h)][\ln t + U(\eta h)] = 0, \quad (11)$$

where $t = T/T_c$, $h = H_{c2}D_1/2\Phi_0T$, $a_0 = 2\omega/\lambda_0$, $a_1 = 1 + \lambda_-/\lambda_0$, and $a_2 = 1 - \lambda_-/\lambda_0$, $\lambda_\pm = \lambda_{11} \pm \lambda_{22}$, $w = \lambda_{11}\lambda_{22} - \lambda_{12}\lambda_{21}$, $U(x) = \psi(1/2 + x) - \psi(1/2)$, and $\lambda_0 = \sqrt{\lambda_-^2 + 4\lambda_{12}\lambda_{21}}$. The function $\psi(x)$ represents the digamma function, λ_{11} and λ_{22} correspond to the intraband coupling constants, λ_{12} and λ_{21} represent the interband coupling constants, and Φ_0 is the magnetic flux quantum. $\eta = D_2/D_1$, D_i is the diffusivity of band i . When the diffusivities are equal ($\eta = 1$), Eq. (10) simplifies to $\ln t + U(h) = 0$, which describes H_{c2} for one-gap dirty superconductors, equivalent to the WHH model in the dirty limit without paramagnetic effects or spin-orbit scattering. The shape of the $H_{c2}(T)$ curve primarily depends on the ratio of the intraband electron diffusivities D_1 (electron diffusivities) and D_2 (hole diffusivities), as shown in Fig. 1. The evolution of the temperature dependence of $H_{c2}(T)$ is evident, transitioning from one-band dirty-limit behavior at $D_1 = D_2$ to distinct $H_{c2}(T)$ curves. For $D_1 \gg D_2$, the curve exhibits a concave shape

near T_c , whereas for $D_1 \ll D_2$, an upward curvature is observed at lower temperatures.

When interband coupling is neglected ($\lambda_{12}=0$), Eq. (10) separates into two independent WHH equations [6, 23, 24]. For the first type of carriers with diffusion coefficient $D = D_1$, the equation becomes:

$$\ln(t^1) + U(\eta) = 0,$$

where $t^1 = T/T_c^1$, $T_c^1 \sim \exp(-1/\lambda_{11})$. For the second type, with $D = D_2$, Eq. (10) yields:

$$\ln(t^1) + U(\eta h) = \lambda_0/\omega,$$

or

$$\ln(t^2) + U(\eta h) = 0,$$

where $t^2 = T/T_c^2$, $T_c^2 \sim \exp(-1/\lambda_{22})$, $\lambda_0/\omega = (\lambda_{11} - \lambda_{22})/(\lambda_{11}\lambda_{22})$ and $T_{c2}/T_{c1} = \exp(-(\lambda_{11} - \lambda_{22})/(\lambda_{11}\lambda_{22}))$, are used [23]. The two-band fitting has been clearly demonstrated in the cuprate high-temperature superconductor $\text{Nd}_{2-x}\text{Ce}_x\text{CuO}_{4+\delta}$, breaking into two independent WHH components, as shown in the following part of Fig. 3(b) [23].

To consider the paramagnetic effect and interband scattering, the dirty-limit two-band WHH model is applied [25, 26]:

$$(\lambda_0 + \lambda_i)[\ln t + U_+] + (\lambda_0 - \lambda_i)[\ln t + U_-] + 2w[\ln t + U_+][\ln t + U_-] = 0, \quad (12)$$

where $\lambda = \lambda_{11}\lambda_{22}$, $w = \lambda_{11}\lambda_{22} - \lambda_{12}\lambda_{21}$, $\lambda_0 = (\lambda_-^2 + 4\lambda_{12}\lambda_{21})^{1/2}$, $\gamma_{\pm} = \gamma_{12} \pm \gamma_{21}$, $\lambda_i = [(w_- + \gamma_-)\lambda_- - 2\lambda_{12}\gamma_{21} - 2\lambda_{21}\gamma_{12}]/\Omega_0$, $2\Omega_{\pm} = w_+ + \gamma_{\pm}\Omega_0$, $\Omega_0 = [(w_- + \gamma_-)^2 + 4\gamma_{12}\gamma_{21}]^{1/2}$, $w_{\pm} = [(D_1 \pm D_2)\pi\hbar H_{c2}]/\phi_0$, $U_{\pm} = \text{Re}\psi(1/2 + (\Omega_{\pm} + i\mu_{eff}H_{c2})/2\pi k_B T) - \psi(1/2)$. Here $\gamma_{mm'}$ are the inter-band scattering rates and μ_{eff} is the electronic effective magnetic moment.

Finally, considering both orbital and paramagnetic depairing effects, the clean-limit two-band WHH model is examined for completeness [27]:

$$(\ln t + U_1(h))(\ln t + U_2(\eta h)) + a_1(\ln t + U_1(h)) + a_2(\ln t + U_2(\eta h)) = 0 \quad (13)$$

$$U_1 = 2e^{a^2} \text{Re}\Sigma_0^{\infty} \int_q^{\infty} du e^{-u^2} \left(\frac{u}{n + \frac{1}{2}} - \frac{t}{\sqrt{b}} \tan^{-1} \left[\frac{u\sqrt{b}}{t(n + \frac{1}{2}) + i\alpha_1 b} \right] \right),$$

$$U_2 = 2e^{a^2 s} \text{Re}\Sigma_0^{\infty} \int_{q\sqrt{s}}^{\infty} du e^{-u^2} \left(\frac{u}{n + \frac{1}{2}} - \frac{t}{\sqrt{b\eta}} \tan^{-1} \left[\frac{u\sqrt{b\eta}}{t(n + \frac{1}{2}) + i\alpha_2 b} \right] \right),$$

$$b = \frac{\hbar^2 v_1^2 H_{c2}}{8\pi\phi_0 k_B^2 T_c^2}, \alpha_i = \frac{4\mu_i \phi_0 k_B T_c}{\hbar^2 v_i^2}, q^2 = \frac{Q^2 \phi_0 \varepsilon_1}{2\pi H_{c2}},$$

$$\eta = \frac{v_2^2}{v_1^2}, S = \frac{\varepsilon_2}{\varepsilon_1},$$

where $a_1 = (\lambda_0 + \lambda_-)/2w$, $a_2 = (\lambda_0 - \lambda_-)/2w$, $\lambda_{\pm} = \lambda_{11} \pm \lambda_{22}$, $w = \lambda_{11}\lambda_{22} - \lambda_{12}\lambda_{21}$, and $\lambda_0 = \sqrt{\lambda_-^2 + 4\lambda_{12}\lambda_{21}}$. Here, v_i represents the in-plane Fermi velocity for band i , ε_i denotes the mass anisotropy ratio ($\varepsilon_i = m_i^{\perp}/m_i^{\parallel}$), μ_i is the effective magnetic moment of the electron, Q stands for the Fulde-Ferrell-Larkin-Ovchinnikov (FFLO) wave vector.

2.4. Anisotropy of H_{c2}

The study of the angle dependence of H_{c2} is important, as it provides crucial insights into the anisotropy of superconductivity and the superconducting order parameter [28]. For three-dimensional (3D) bulk superconductors, the angle dependence of H_{c2} can be described by the GL model using the following formula [29, 30]:

$$H_{c2}(\theta) = H_{c2}^{ab} / \sqrt{\cos^2 \theta + (H_{c2}^{ab}/H_{c2}^c)^2 \sin^2 \theta}. \quad (14)$$

The polar angle θ represents the angle between the magnetic field and the ab -plane. The Tinkham model describes the behavior of $H_{c2}(\theta)$ in two-dimensional systems, which satisfy the condition that the out-of-plane coherence length is larger than the thickness of the superconducting layer (d_{SC}):

$$\left| \frac{H_{c2}(\theta) \sin \theta}{H_{c2}^c} \right| + \left(\frac{H_{c2}(\theta) \cos \theta}{H_{c2}^{ab}} \right)^2 = 1. \quad (15)$$

This model accounts for the cusplike behavior observed near parallel magnetic fields, a characteristic commonly seen in various 2D systems [30, 31]. It is important to note that the 2D Tinkham model assumes that $H_{c2}(\theta)$ is entirely governed by orbital effects across the entire angular range.

3. The upper critical field of Cuprate

The discovery of cuprate high-temperature superconductors dates back to 1986, with Bednorz and Müller reporting superconductivity at a T_c exceeding 30 K in $\text{La}_{2-x}\text{Ba}_x\text{CuO}_4$. This groundbreaking discovery rapidly stimulated a worldwide effort to explore high-temperature superconductivity. One year later, superconductivity with T_c reaching 90 K was discovered in the

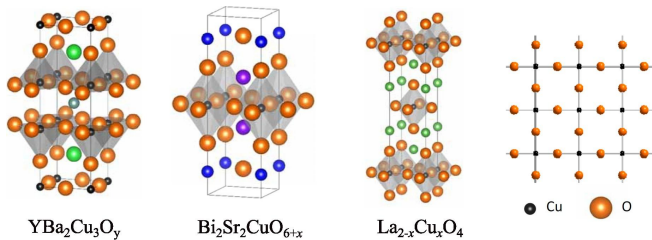


FIG. 2. Schematic crystal structure of several representative cuprates

Y-Ba-Cu-O system [32], marking a significant milestone as the critical temperature exceeded the boiling point of liquid nitrogen (77 K). Cuprate high-temperature superconductors feature a layered perovskite structure with pronounced two-dimensional characteristics, consisting mainly of CuO_2 planes acting as conducting layers, interleaved with insulating layers serving as charge reservoirs, as illustrated in Fig. 2.

3.1. The temperature dependence of H_{c2} in cuprate

For cuprate superconductors, the temperature dependence of H_{c2} shows that the $H_{c2}^{ab}(T)$ curve displays a convex trend, whereas the $H_{c2}^c(T)$ curve exhibits either a more linear or concave dependence near T_c , such as $\text{Sr}_{1-x}\text{La}_x\text{CuO}_2$ [33], $\text{Pr}_{2-x}\text{Ce}_x\text{CuO}_{4-y}$ (PCCO) [34], $\text{Nd}_{2-x}\text{Ce}_x\text{Cu}_{4+\delta}$ (NCCO) [23, 35], and $\text{Bi}_2\text{Sr}_2\text{CuO}_{6+\delta}$ (2201) [36]. Here, H_{c2}^{ab} and H_{c2}^c represent the upper critical fields when the magnetic field is applied in the ab -plane and along the c -axis, respectively.

Fig. 3(a) presents the temperature dependence of H_{c2} for an optimally doped $\text{YBa}_2\text{Cu}_3\text{O}_{7-\delta}$ (YBCO) thin sample, measured using a contactless radio frequency transmission technique (RF method) [32]. The single-band WHH fitting can effectively describe the behavior of $H_{c2}(T)$. For $H_{c2}^{ab}(T)$, the Maki parameter α_M and spin-orbit scattering λ_{so} obtained from the fitting are 5.1 and 1.5, indicating that the spin paramagnetic pair breaking effect is dominant. When $(\alpha_M, \lambda_{\text{so}}) = (0, 0)$, the WHH model can also effectively fit the behavior of $H_{c2}^c(T)$, suggesting that the pair-breaking is solely caused by the orbital-limiting effect. In general, most cuprate superconductors are single-band systems that can be effectively characterized by the WHH model. However, in electron-doped superconducting NCCO single crystals [35] and thin films [23, 37, 38], the anomalous upward curvature observed in $H_{c2}^c(T)$ cannot be well described by the WHH model. When attempting to describe the $H_{c2}(T)$ using two independent WHH equations based on Eq. (11) with $\lambda_{12} = 0$, as shown in Fig. 3(b), it can be observed that the behavior results from a superposition of WHH curves for two types of carriers (electrons and holes), each associated with different critical fields, H_{c2}^1

and H_{c2}^2 , as well as different transition temperatures, T_c^1 and T_c^2 . Therefore, the two-band model effectively captures the essence of the $H_{c2}(T)$ behavior for NCCO.

3.2. Anisotropy of H_{c2} in cuprate

Due to their unique layered structure, cuprate superconductors exhibit a considerable distance between the CuO_2 planes and the charge reservoir layers, resulting in significant anisotropy. Fig. 4(a) presents a schematic illustration of the angles, where φ represents the rotation angle of the magnetic field within the ab plane, and θ represents the angle between the magnetic field and the c axis. In Bi2201 superconductors, it can be observed that H_{c2} exhibits a cusplike behavior at $\theta = 90^\circ$ (see Fig. 4(b)). Therefore, the 2D Tinkham model can be used to describe the angular dependence of H_{c2} . The dashed lines in Fig. 4(c) represent the Tinkham fit, which aligns well with the expected characteristics of conventional two-dimensional layered superconductors. In contrast to conventional superconductors, cuprates exhibit an anisotropic superconducting gap with d -wave pairing symmetry. This is also reflected in their transport properties. The in-plane angular dependence of the upper critical field manifests as a fourfold symmetry, as observed in $\text{La}_{1.45}\text{Nd}_{0.4}\text{Sr}_{0.15}\text{CuO}_4$ (see Fig. 4(c)).

3.3. The doping dependence of H_{c2} in cuprate

Fig. 5 illustrates the H_c of YBCO, LSCO, Bi2201, and $\text{Bi}_2\text{Sr}_2\text{CaCu}_2\text{O}_8$ (Bi2212) as a function of doping (p/x) under different magnetic fields [41–43]. Clearly, the $H_{c2}(p)$ of YBCO and LSCO show variations that align with changes in $T_c(p)$. Additionally, the H - p phase diagram of superconductivity in YBCO features two distinct peaks, positioned at $p_1 \approx 0.08$ and $p_2 \approx 0.18$. Strong evidence indicates the presence of two distinct phase transitions in YBCO — one occurring at p_1 , and the other at a critical doping level corresponding to p_2 [44]. Notably, the Fermi surface is observed to undergo a transformation at $p = 0.08$ and another near $p \approx 0.18$ [45]. Constructing the H - p (or H - x) phase diagram provides a way to identify the locations of these quantum critical points (QCPs). A similar behavior has also been observed in iron-based superconductors. In contrast, for Bi2201 and Bi2212, different behaviors are observed in the H_{c2} and T_c as functions of doping concentration [43]. The observed increase in H_{c2} with decreasing doping concentration (x) suggests that the superconducting pairing strength is enhanced in underdoped samples. This behavior contrasts with the trend of the superfluid density, which generally decreases as doping is reduced [46, 47]. The increase in H_{c2} indicates that the pairing potential remains robust in the underdoped regime, despite the

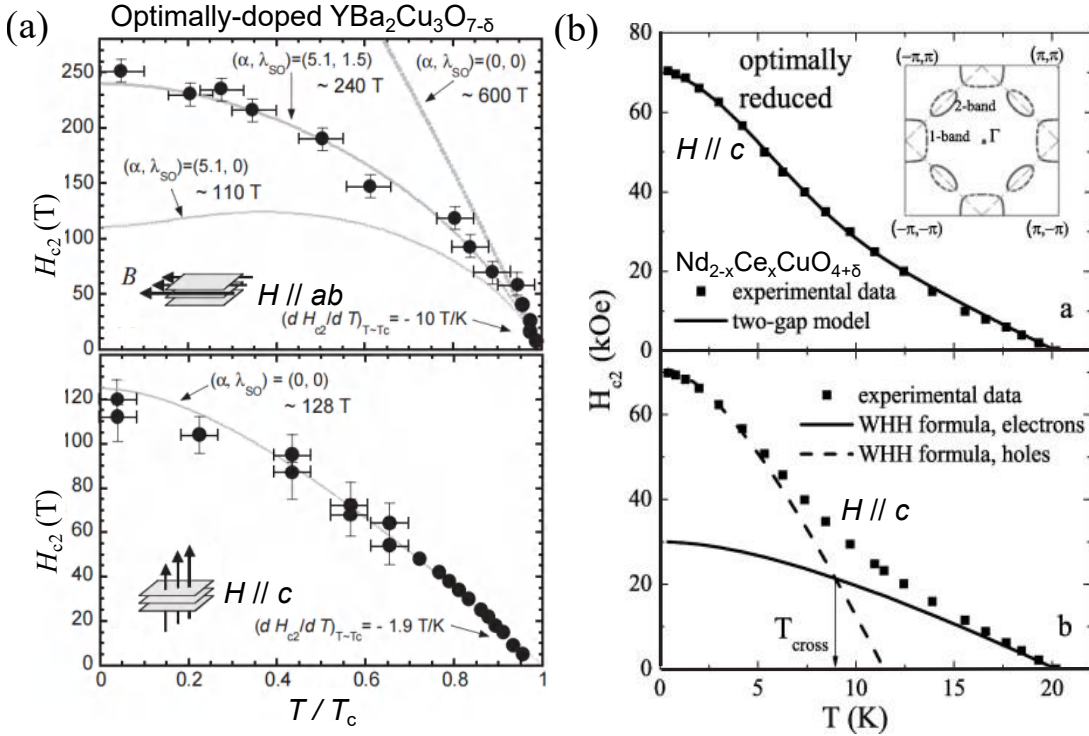


FIG. 3. (a) $H_{c2}(T)$ for optimally doped YBCO single crystal under $H \parallel ab$ (parallel to the CuO_2 plane, upper) and $H \parallel c$ (perpendicular to the CuO_2 plane, lower). The dashed lines correspond to the single-band WHH fitting curves [32]. (b) Temperature dependence of H_{c2} for an optimally reduced $\text{Nd}_{1.85}\text{Ce}_{0.15}\text{CuO}_4$ film with $H \parallel c$. The solid line represents the two-band model fitting. In the lower panel, the solid and dashed lines represent fits based on the electron single-band and hole single-band WHH models, respectively [23].

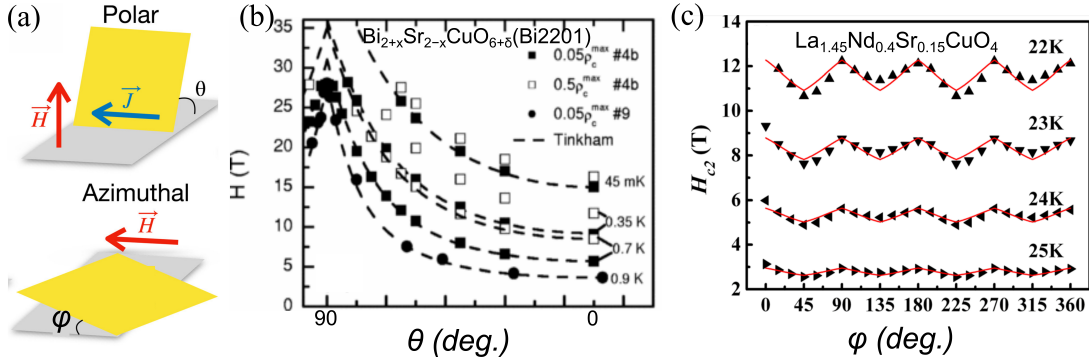


FIG. 4. (a) Schematic of the measurement geometry relative to the sample (yellow square). (b) $H_{c2}(\theta)$ at different temperatures ranging from 45 mK to 0.9 K for Bi2201 [39]. (c) $H_{c2}(\phi)$ at different temperatures for $\text{La}_{1.45}\text{Nd}_{0.4}\text{Sr}_{0.15}\text{CuO}_4$ [40].

reduced carrier density. It is believed that the superconducting dome is determined by both pairing strength and superfluid density.

4. The upper critical field of FeSCs

In 2008, the discovery of superconductivity in $\text{LaO}_{1-x}\text{F}_x\text{FeAs}$ at 26 K stimulated the widespread interest in high-temperature FeSCs [3]. In comparison to cuprate superconductors, the layered crystal structure,

the antiferromagnetic order in the parent compounds (though with different AFM configurations), and the distinct band structures make FeSCs an important platform for investigating high-temperature superconductivity mechanisms. So far, four main categories of FeSCs have been classified based on the crystal structures of their stoichiometric parent compounds, as illustrated in Fig. 6: the 11-type (FeTe, FeSe, FeS), the 111-type (AFeAs, where A represents an alkali metal), the 122-type (AeFe_2As_2 , with Ae being Ba, Sr, K, or Ca), and the

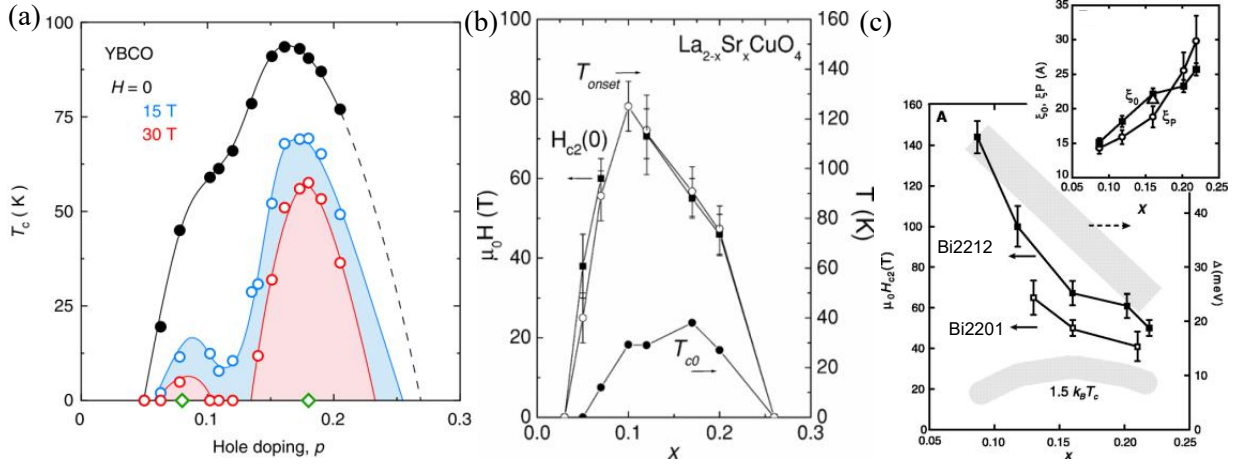


FIG. 5. (a) T_c of YBCO as a function of doping (p) at different magnetic field values (H) [41]. T_c is determined at zero resistance. Two peaks are observed in H_{c2} and in superconducting phase diagram, located at $p=0.08$ and $p=0.18$. (b) $H_{c2}(0)$ as a function of x in LSCO (solid squares). $H_{c2}(0)$ values are extrapolated from measurements up to 45 T [42]. (c) The x dependence of H_{c2} in Bi 2212 (solid squares) and in Bi 2201 (open squares) measured by scaling of Nernst profiles. The upper gray stripe represents the x dependence of the ARPES gap Δ_0 , while the lower gray stripe represents T_{c0} . The inset shows a comparison of the coherence length ξ_0 (solid squares) obtained from H_{c2} and the Pippard length ξ_P (open circles) obtained from Δ_0 [43].

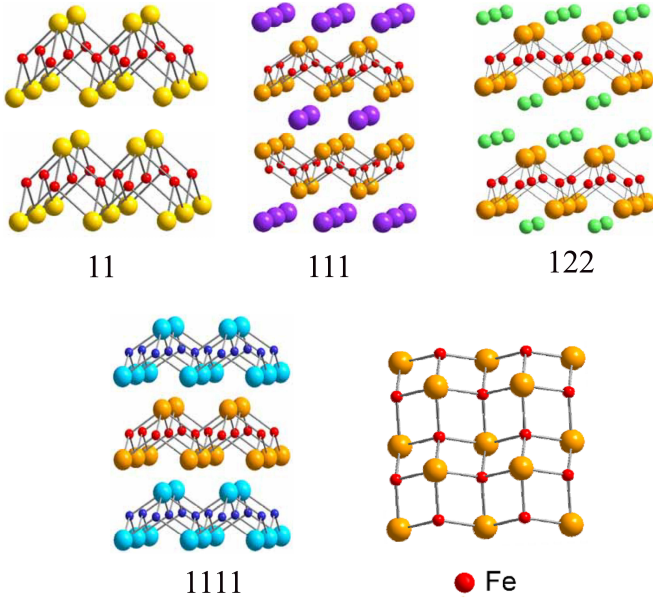


FIG. 6. Schematic crystal structure of several representative FeSCs

1111-type (LnOFeAs , where Ln denotes a rare-earth element). High-temperature superconductivity originates from the FeSe/FeAs layers, similar to the CuO planes in cuprate high-temperature superconductors.

4.1. The temperature dependence of H_{c2} in FeSCs

Iron-based superconductors exhibit relatively high H_{c2} , with distinct temperature dependencies due to different contributions from multiband effects and spin-paramagnetic effects. Fig. 7 shows several typical temperature dependencies of $H_{c2}(T)$ in iron-based superconductors. Specifically, in iron chalcogenide (FeCh) superconductors (FeSe) [48], for $H \parallel c$, the temperature dependence of $H_{c2}(T)$ is nearly linear, with a slight upturn at low temperatures. The value of H_{c2} significantly exceeds the predicted upper limit based on the WHH theory [20], where both the Maki parameter α_M and the spin-orbit interaction λ are zero, as shown by the black lines in Fig. 7(a). In contrast, for $H \parallel ab$, the $H_{c2}(T)$ curve shows a convex shape, tending to saturate at low temperatures, with values falling below the WHH prediction at low temperatures when $\alpha = 0$ and $\lambda = 0$, indicating that the spin-paramagnetic effect cannot be neglected. Similarly, the $H_{c2}(T)$ curves in Ba-122 [53] and LiFeAs [50] exhibit comparable characteristics, with WHH fitting revealing relatively large Maki parameters, as illustrated in Figs. 7(c) and (e). However, in the FePn-1111 system (LnFeAs(O,F)) [6], the behavior is notably different, as illustrated in Fig. 7(f). $B_{\text{min}}(T)$ and $B_{\text{max}}(T)$ represent $H_{c2}^c(T)$ ($H \parallel c$) and $H_{c2}^{ab}(T)$ ($H \parallel ab$), respectively. $H_{c2}^c(T)$ exhibits a linear increase as the temperature decreases near T_c , followed by a distinct upward curvature. This behavior can be explained by a two-band theory and is reminiscent of MgB_2 , which provided the first experimental evidence for two-band superconductivity in FeSCs [?]. The hypothesis of multi-band superconductivity was

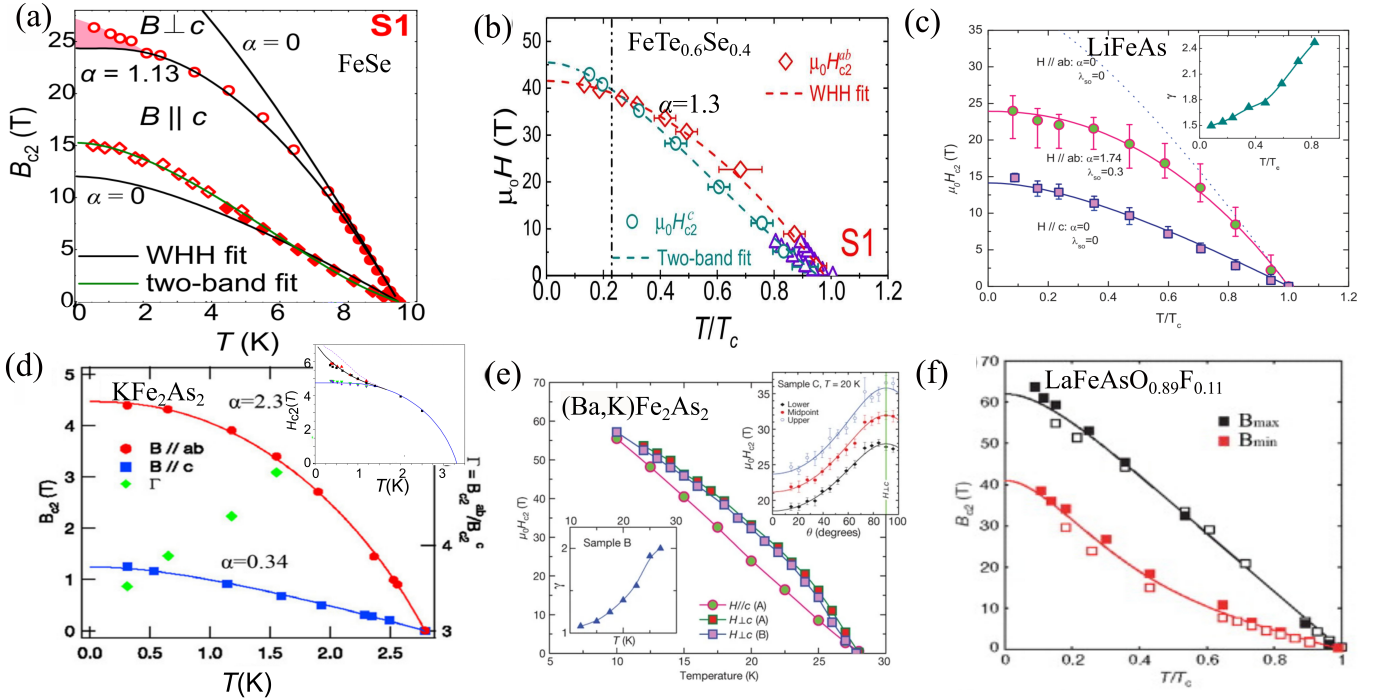


FIG. 7. The temperature dependence of H_{c2} for FeSe [48], $\text{FeTe}_{0.6}\text{Se}_{0.4}$ [49], LiFeAs [50], KFe_2As_2 [51, 52], $(\text{Ba},\text{K})\text{Fe}_2\text{As}_2$ [53], and $\text{LaFeAsO}_{0.89}\text{F}_{0.11}$ [6]. The solid and dashed lines in the Figs. (a-c) and (e-f) represent fitted curves, either WHH fitting or two-band fitting.

later confirmed by ARPES experiments [54].

In FeSCs, WHH fitting typically yields a large Maki parameter, suggesting that the spin-paramagnetic effect is dominant. When α_M is sufficiently large and the superconductors are in the clean limit, the Fulde–Ferrell–Larkin–Ovchinnikov (FFLO) state may appear, leading to non-zero momentum of Cooper pairs and spatial oscillations of the superconducting order parameter. Fig. 7(a) clearly shows that in FeCh-FeSe superconductors, the Pauli limit is significantly exceeded, accompanied by an upward curvature in $H_{c2}(T)$. Generally, for a conventional s -wave superconductor, the FFLO state is known to be highly sensitive to nonmagnetic disorder, existing only in crystals under the clean limit conditions [55, 56]. For H_{c2}^{ab} in FeSe, an unusual superconducting phase was observed at low temperatures across all crystals, regardless of varying levels of disorder [48]. This finding indicates that the high-field superconducting phase in FeSe does not exhibit the typical characteristics of a conventional FFLO state. However, theoretical calculations suggest that the FFLO state may be less vulnerable to disorder in unconventional superconductors, such as disordered s -wave [57] or d -wave superconductors [58, 59]. In addition to the FFLO state, spin density wave (SDW) order has also been considered as a potential mechanism for the high-field superconducting phase in the heavy-fermion superconductor CeCoIn_5 . Theoretical calculations suggest that the SDW order near H_{c2} is

driven by a strong spin-paramagnetic pair-breaking effect combined with the nodal gap structure. In FeSe, both the electron-type band, which exhibits a small gap, and the hole-type band, with a larger gap, show gap nodes or deep minima, facilitating the possibility of field-induced SDW order. In addition, the multi-band effect in iron-based superconductors is also one of the possible origins of the upturn in the upper critical field. To better understand the origin of the high-field superconducting phase in FeSe, further studies, including nuclear magnetic resonance and neutron diffraction, are crucial.

In FePn-122 superconductors, an upward curvature in the upper critical field has also been observed, as shown in the inset of Fig. 7(d) [51]. Thermodynamic evidence for an FFLO state in KFe_2As_2 was obtained by investigating its $H - T$ phase diagram near the Pauli limit using magnetic torque (τ) and specific heat (C_p) measurements. Notably, only under strict alignment conditions does the magnetic field lead to a distinctive upturn in $H_{c2}(T)$, surpassing the conventional Pauli limit. It also revealed a double transition, indicating a sequence from a homogeneous superconducting state to the FFLO state and finally to the normal state. This finding is crucial as it suggests the existence of a highly unconventional superconducting phase.

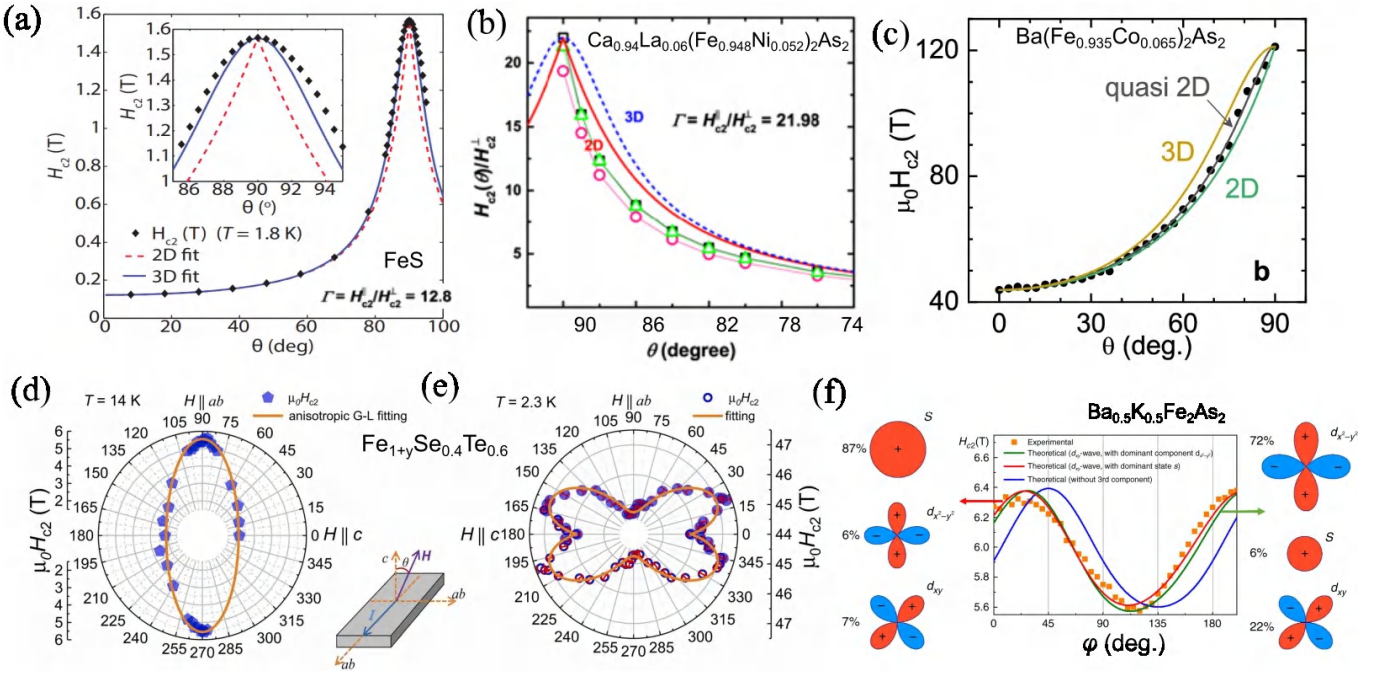


FIG. 8. The angle dependence of the upper critical field $H_{c2}(\theta)$ for FeS [60], $\text{Ca}_{0.94}\text{La}_{0.06}(\text{Fe}_{0.948}\text{Ni}_{0.052})_2\text{As}_2$ [61], and $\text{Ba}(\text{Fe}_{0.935}\text{Co}_{0.065})_2\text{As}_2$ [15]. Angle dependent of H_{c2} at $T=14$ K (d) and 2.3 K (e) for $\text{Fe}_{1+y}\text{Se}_{0.4}\text{Te}_{0.6}$ [49]. (f) In-plane angle dependence of $H_{c2}(\varphi)$ at 38.4 K for $\text{Ba}_{0.5}\text{K}_{0.5}\text{Fe}_2\text{As}_2$ [62].

4.2. Anisotropy of H_{c2} in FeSCs

In FeCh-FeS superconductors, the angle dependence of H_{c2} at 1.9 K with respect to θ is illustrated in Fig. 8(a) [60]. The 3D GL model provides a significantly better fit for the $H_{c2}(\theta)$ curve compared to the 2D Tinkham model. The anisotropy parameter Γ is 12.8, indicating a strongly anisotropic three-dimensional superconducting environment in FeS. However, in FePn-122 superconductors, a cusplike behavior near $\theta = 0^\circ$ is observed in the $H_{c2}(\theta)$ curves, as depicted in Figs. 8(b)-(c) [61]. For FeCh-FeS, the interlayer distance is ~ 5.034 Å, and the coherence length along the c axis (ξ_c) is around 343 Å. In contrast, FePn- $\text{Ca}_{0.94}\text{La}_{0.06}(\text{Fe}_{0.948}\text{Ni}_{0.052})_2\text{As}_2$ has a c -axis coherence length (ξ_c) ranging from about 3 to 16 Å and for $\text{Ba}(\text{Fe}_{0.935}\text{Co}_{0.065})_2\text{As}_2$, ξ_c (0 K) is ~ 10 Å. In $\text{Bi}_{2.2}\text{Sr}_2\text{Ca}_{0.8}\text{Cu}_2\text{O}_{8+\delta}$, the distance between adjacent superconducting layers reaches ~ 12 Å, significantly exceeding the coherence length ξ_c (~ 1.6 Å). These observations indicate that a large interlayer distance and a short coherence length along the c -axis are crucial factors contributing to the occurrence of two-dimensional superconductivity [61]. Furthermore, in the insets of Figs. 7(c) and 7(e), the temperature dependence of H_{c2} anisotropy parameter for FePn-111 (LiFeAs) and FePn-122 ($(\text{Ba},\text{K})\text{Fe}_2\text{As}_2$) is also shown. The anisotropy ratio Γ trends towards isotropy as the temperature decreases. $(\text{Ba},\text{K})\text{Fe}_2\text{As}_2$ was the first iron-based superconductor found to be near isotropy. This discovery is

particularly significant, as it demonstrates that its superconducting properties increasingly resemble 3D behavior at lower temperatures, which is beneficial for potential applications.

In Fig. 7(b), a crossover between the $H_{c2}^c(T)$ and $H_{c2}^{ab}(T)$ curves for $\text{FeSe}_{0.6}\text{Te}_{0.4}$ is observed [49]. This crossover is notably robust against disorder. Similar unusual behavior has also been reported in other compounds, including $\text{Ba}_{1-x}\text{K}_x\text{Fe}_2\text{As}_2$ [53], ACr_3As_3 [63], and $\text{A}_2\text{Cr}_3\text{As}_3$ [64, 65], where A represents an alkali metal. Figs. 8(d)-(e) present the angular dependence of H_{c2} in $\text{FeSe}_{0.6}\text{Te}_{0.4}$ at 14 K (above the crossover point) and 2.3 K (below the crossover point) for the out-of-plane direction, respectively [49]. The behavior of $H_{c2}(\theta)$ above and below the crossover point in $\text{FeSe}_{0.4}\text{Te}_{0.6}$ exhibits an evolution from twofold (C2) to fourfold (C4) symmetry. A spin-orientation-locking model in quasitwo-dimensional superconductors is proposed to explain the observed behavior. This model introduces the concept of half-itinerant carriers, whose spins are confined within the ab -plane, while both charge and spin remain itinerant. For $H \parallel ab$ -plane, an angle between the magnetic field and the spins in a Cooper pair leads to additional magnetization energies of $+|M \cdot H|$ and $-|M \cdot H|$, leading to a peak in depairing energy. When the magnetic field is applied along the c -axis, perpendicular to the spin directions, the magnetization energy remains zero, and no spin-paramagnetic depairing effects occur. Furthermore, both orbital depairing and spin-paramagnetic

depairing effects depend on the angle θ . As the magnetic field rotates from $H \parallel c$ to $H \parallel ab$, the rate of attenuation for orbital depairing effects surpasses the rate of enhancement for in-plane spin-paramagnetic depairing effects. However, the general applicability of this theoretical model requires further validation across different types of iron-based superconductors.

For FePn-122, Fig. 8(c) clearly shows that the out-of-plane angular dependence of H_{c2} exhibits C2 symmetry, consistent with the typical characteristics of layered superconductors. Fig. 8(f) illustrates the in-plane angular dependence of H_{c2} at 38.4 K (close to $T_c \approx 39$ K) for FePn-122 ($\text{Ba}_{0.5}\text{K}_{0.5}\text{Fe}_2\text{As}_2$) [62]. In the superconducting phase diagram of $\text{Ba}_{1-x}\text{K}_x\text{Fe}_2\text{As}_2$, the nematic phase can be observed and persists until it vanishes at $x \approx 0.3$. Electronic nematic order is commonly observed in other unconventional superconductors, including high- T_c cuprates and heavy-fermion compounds. It is characterized by the breaking of tetragonal rotational symmetry, often leading to a structural transition to an orthorhombic phase. Based on the behavior of $H_{c2}(\phi)$, it is evident that the C2 symmetry of the superconducting condensate persists from the onset of superconductivity to low temperatures and across a range of dopings around $x = 0.5$, indicating that the nematic state is present over a broad doping range. Notably, this nematic order is not accompanied by the typical tetragonal symmetry breaking of the crystal lattice or the emergence of magnetic order, making it an unusual characteristic among iron-based superconductors. The unusual nematic state is thought to arise from the weak coupling between the quasi-degenerate $s\pm$ -wave and d -wave components in the superconducting condensate.

4.3. The doping dependence of H_{c2} in FeSCs

Fig. 9 presents the T_c phase diagram of $\text{FeSe}_{1-x}(\text{Te}/\text{S})_x$ under different magnetic fields [66]. At $H = 0$, the doping of S and Te results in the appearance of two distinct superconducting domes. The nematic transition temperature T_s gradually decreases with increasing doping and eventually vanishes around $x(\text{S}) \sim 0.17$ and $x(\text{Te}) \sim 0.5$. Systematic elastoresistivity measurements on $\text{FeSe}_{1-x}\text{Te}_x$ single crystals identified a non-magnetic nematic QCP at $x \sim 0.5$, isolated from any other long-range orders, located at the center of the superconducting dome [67]. As the magnetic field increases, the superconducting dome for $\text{FeSe}_{1-x}\text{Te}_x$ contracts into a narrower dome around the nematic QCP. Similar behavior has also been observed in cuprate superconductors, as mentioned in the previous section. Analysis of H_{c2} reveals that the Pauli-limiting field increases as the system nears the QCP, indicating that the pairing interaction is significantly enhanced by nematic fluctuations emanating from the QCP. The dependence of H_{c2} on doping plays

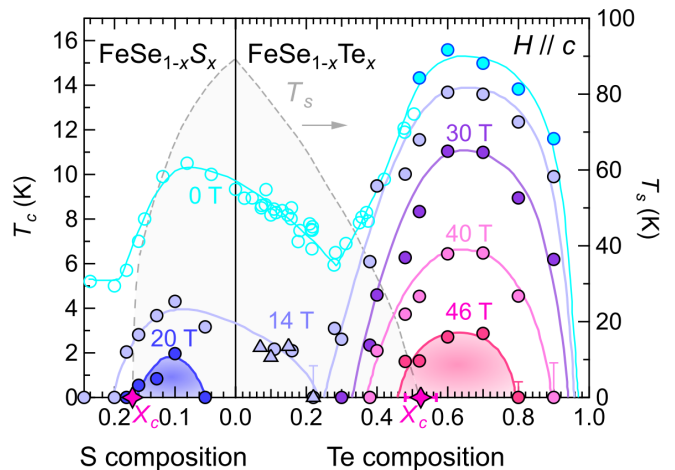


FIG. 9. Superconducting phase diagram of $\text{FeSe}_{1-x}(\text{Te}/\text{S})_x$ under different magnetic fields. The gray dashed line indicates zero-temperature intercepts of the structural transition T_s , and x_c represents the nematic quantum critical points [66].

a crucial role in exploring QCPs. However, $\text{FeSe}_{1-x}\text{S}_x$ exhibits a QCP associated with magnetic ordering. Unlike $\text{FeSe}_{1-x}\text{Te}_x$, the superconducting dome in $\text{FeSe}_{1-x}\text{S}_x$ does not contract around the QCP as the magnetic field increases, likely due to the influence of spin fluctuations. Further research is essential to achieve a more profound understanding.

5. The upper critical field in infinite-layer nickelate superconductors

In 2021, superconductivity was first observed in infinite-layer nickelate films — $\text{Nd}_{1-x}\text{Sr}_x\text{NiO}_2$ [4]. Subsequently, the development of rare-earth (R) variants, substituting Nd with Pr or La, has led to the emergence of a new family of superconducting infinite-layer nickelates. The films undergo a topotactic transition from the perovskite phase to the infinite-layer phase, as shown in Fig. 10. These infinite-layer nickelate superconductors are not only isostructural to the well-known cuprate superconductor CaCuO_2 , but also feature Ni and Cu with a similar formal $3d^9$ electronic configuration in their respective parent compounds.

5.1. The temperature dependence of H_{c2} in infinite-layer nickelate superconductors

The temperature dependence of H_{c2} for $R_{1-x}\text{Sr}_x\text{NiO}_2$ thin films was investigated by measuring resistivity in both inter-plane ($H \parallel c$) and in-plane ($H \parallel ab$) directions under magnetic fields [30, 68, 69]. As shown in Fig. 11, the $H_{c2}(T)$ behavior of nickelate superconductors containing different rare-earth elements exhibits several com-

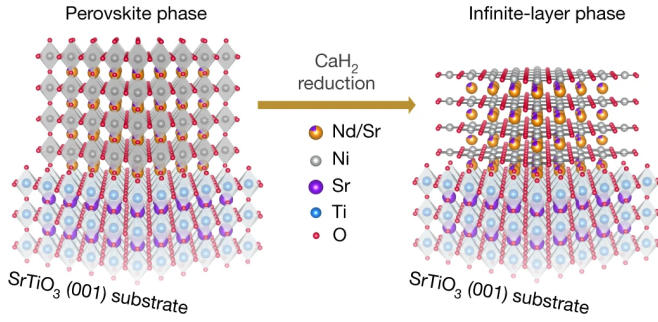


FIG. 10. (a) Topotactic reduction of nickelate thin films [4]

mon characteristics: (1) anomalous low-temperature upturn; (2) square-root temperature dependence of H_{c2}^{ab} ; (3) linear temperature dependence of H_{c2}^c . Additionally, notable differences in anisotropy have also been observed.

The linear temperature dependence of H_{c2}^c in all nickelate thin films can be interpreted as indicating a dominant orbital depairing effect near T_{c0} , which fits well with the two-band model. Similar behavior has also been observed in most iron-based superconductors [50, 53, 70, 71]. For H_{c2}^{ab} , a $(T_c - T)^{1/2}$ temperature dependence is observed in La-, Pr-, and Nd-nickelate superconductors, which is similar to the behavior predicted by the GL model for thin films [72]:

$$H_{c2}^{ab}(T) = \frac{\sqrt{12}\phi_0}{2\pi\xi_{ab}(0)d_f} \left(1 - \frac{T}{T_{c0}}\right)^{1/2},$$

where d_f is the film thickness. However, the deduced superfluid thickness shows an unphysical discrepancy consistently across all samples, indicating that the orbital depairing effect alone cannot fully explain the temperature dependence of H_{c2}^{ab} . This necessitates consideration of the paramagnetic depairing effect. Within the pair-breaking framework proposed by Abrikosov-Gorkov [73, 74], $\ln(T/T_{c0}) = \psi(1/2) - \psi(1/2 + \alpha_M/2\pi k_B T_{c0})$. When considering only the orbital depairing effect, it is characterized by $\alpha_M = D^{ab}eH/c$, where e is the electronic charge, c is the speed of light, and D^{ab} is the in-plane electronic diffusion coefficient. The $H_{c2}^c(T)$ derived from this term indeed exhibits a linear temperature dependence near T_{c0} . On the other hand, when considering only the paramagnetic effect, it can be described by $\alpha_M = \frac{\tau_{so}e^2\hbar H^2}{2m_{eff}^2 f f}$ [74], where τ_{so} is the spin-orbit scattering time and m_{eff} is the electronic effective mass. Maki and Tsuneto [75] derived an approximation for the temperature dependence of H_{c2} in the limit of $T - T_{c0} \ll T_{c0}$, expressed as $-\ln(T/T_{c0}) = 7\zeta(3)(\mu_{eff}H/2\pi T_{c0})^2$, $(\mu_{eff}H)/(2\pi T_{c0}) \ll 1$, which exhibits a $(T_c - T)^{1/2}$ dependence near T_{c0} . Here, ζ is the Riemann zeta function, and μ_{eff} represents the effective magnetic moment. This further validates our analysis of the temperature dependence behavior of H_{c2} in nickelate superconductors.

To reveal the intriguing behavior of the low-temperature upturn, it is necessary to verify it in nickelate thin films under the clean limit. $\text{La}_{0.8}\text{Sr}_{0.2}\text{NiO}_2$ thin films, prepared by the MBE method and exhibiting a macroscopic clean limit, possess a high superconducting transition temperature ($T_c^{\text{onset}} = 18.8$ K) and very large upper critical fields ($H_{c2}^c(0) \approx 40$ T, $H_{c2}^{ab}(0) \approx 52$ T), making them well-suited for studying this issue. By fitting using the WHH model, it is found that the similar low-temperature upturn behavior and a large parameter α^{Maki} were found in all infinite-layer nickelate superconductors. Additionally, the scaling curve of $H_{c2}/H_{c2}^{\text{WHH}}(0$ K) in $\text{La}_{0.8}\text{Sr}_{0.2}\text{NiO}_2$ films with different T_c (i.e., different levels of disorder) shows nearly identical upturn behavior (see Fig. 12(d)), indicating that the anomalous upturn is independent of film quality and rare-earth elements.

The anomalous upturns observed in heavy-fermion superconductors [55, 77], organic superconductors [78], and some iron-based superconductors have been attributed to the FFLO state. However, for conventional s -wave superconductors, the FFLO state is easily destroyed by impurities [55]. Moreover, due to the fact that the film is in the dirty limit, the anomalous upturn behavior observed in nickelates is unlikely to be attributed to the FFLO state. What, then, is the cause of the low-temperature high-field phase? The high-field superconducting phase may originate from the presence of a spin-density wave (SDW). For instance, in the heavy-fermion superconductor CeCoIn_5 , an additional SDW coexists with superconductivity [79, 80]. The hybridization of La $5d$ and Ni $3d$ orbitals enhances the interlayer electron coupling as the temperature decreases, which could induce SDW fluctuations. However, more evidence is needed to confirm the coexistence of SDW and superconductivity. The multiple-band effect could also be a reason for the low-temperature upturn in $H_{c2}(T)$. For La-, Pr- and Nd-nickelates, the distinctions originate from the characteristics of $4f$ electrons in the lattice: La^{3+} has no $4f$ electrons; Pr^{3+} , with a singlet ground state, is non-magnetic, similar to La^{3+} ; while Nd^{3+} is magnetic. Fig. 12(a-b) presents the normalized $H_{c2}(T)$ curves of these $R_{1-x}\text{Sr}_x\text{NiO}_2$ ($R = \text{La}, \text{Pr}, \text{Nd}$) nickelate superconductors [69]. Regardless of the specific doping level, H_{c2} of Nd-nickelate is significantly lower than that of La- and Pr-nickelates. Also noteworthy is that the H_{c2} of La- and Pr-nickelates greatly exceeds the conventional Pauli limit by approximately 3.5 times ($H_{c2} \approx 1.86T_{c0}$). Furthermore, the H_{c2} of Nd- and Pr-nickelates can be scaled onto a single curve through normalization. These observed differences are likely influenced by the presence of $4f$ electrons. The angular dependence of magnetoresistance measurements in La-, Pr-, and Nd-nickelates, as shown in Fig. 13, may provide further insights into the reasons behind the variations in H_{c2} among these materials.

For $R_{1-x}\text{Sr}_x\text{NiO}_2$ ($R = \text{La}, \text{Pr}, \text{Nd}$), the magnetore-

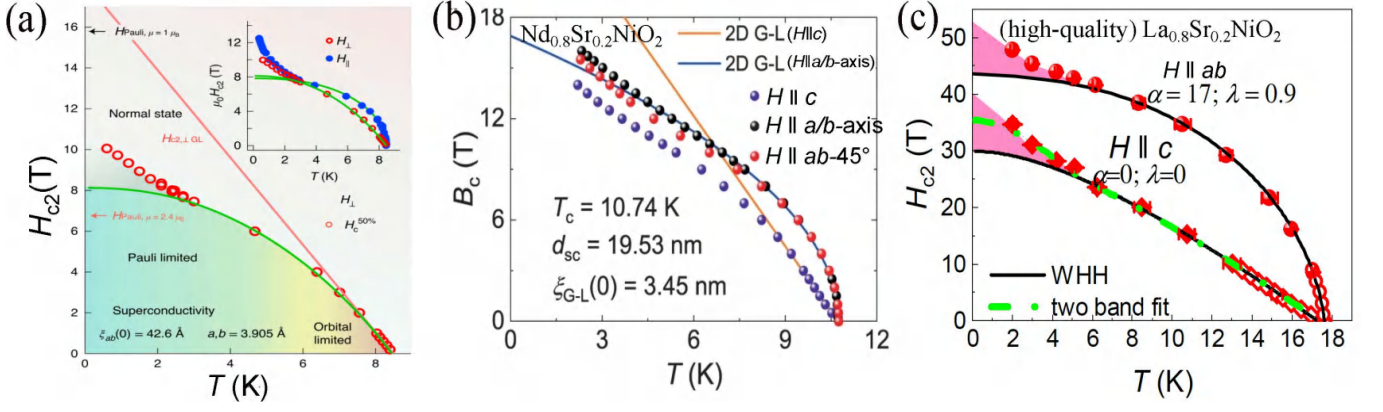


FIG. 11. Temperature dependence of H_{c2} for $H \parallel c$ and $H \parallel ab$ in $R_{1-x}Sr_xNiO_2$ ($R = Nd(a-b), La(c)$), determined using a 50% ρ_n criterion [25, 30, 68].

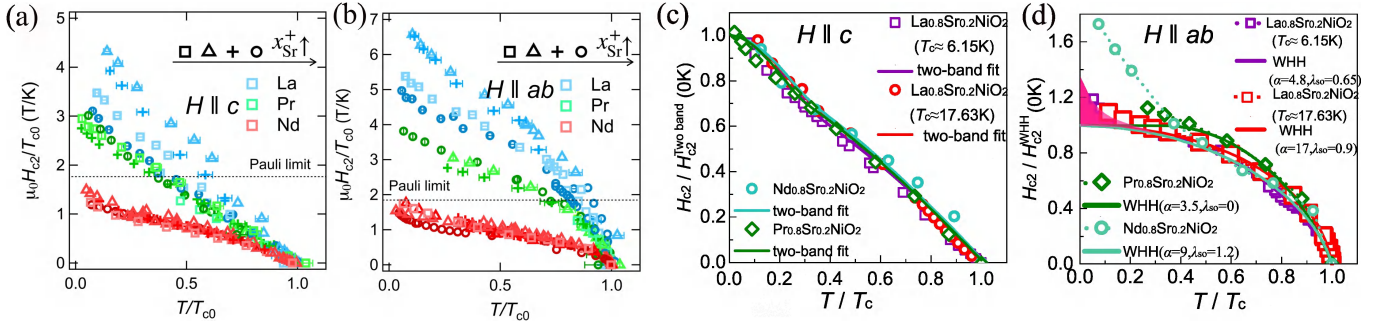


FIG. 12. (a-b) Normalized H_{c2}/T_{c0} against reduced temperature T/T_{c0} of $R_{1-x}Sr_xNiO_2$ for $H \parallel c$ and $H \parallel ab$, respectively. Here, $x = 0.15, 0.175, 0.2$, and 0.225 [25, 69, 76] for Nd, $x = 0.16, 0.18, 0.20$, and 0.24 for Pr, and $x = 0.15, 0.16, 0.18$, and 0.20 for La. The dashed lines indicate the Pauli limit of $H_{c2} = 1.86 T_{c0}$ [69]; (c-d) Normalized $H_{c2}/H_{c2}^{two-band}$ (0 K) and Normalized H_{c2}/H_{c2}^{WHH} (0 K) data for $R_{0.8}Sr_{0.2}NiO_2$ ($R = La, Pr, \text{ or } Nd$) with different rare-earth elements [30].

sistance in both the normal state and fully superconducting state shows no dependence on the polar or azimuthal angles. Thus, only the superconducting transition region is considered. In this region, La- and Pr-nickelates exhibit a typical polar angular dependence. In Figs. 13(a)-13(b), the "∞"-shaped dependence on θ suggests that superconductivity is less suppressed (lower resistance) when the external magnetic field is applied in the plane of NiO_2 , indicating a weaker depairing effect—this is a common characteristic of layered superconductors [81, 82]. The "8"-shaped, two-fold (C_2) symmetric ϕ dependence shown in Figs. 13(e)-13(f) is also consistent with previous studies of other type-II superconductors [82, 83]. In contrast, Nd-nickelate exhibits distinct behavior. The "8"-shaped θ dependence in Fig. 13(c) indicates that superconductivity is more significantly suppressed by the in-plane magnetic field. Additionally, the four-fold (C_4) symmetric ϕ dependence in Fig. 13(g) suggests a potential influence of localized magnetic moments [69]. The anomalous θ dependence in Nd-nickelate can be attributed to the combined effect of two mechanisms: the conventional anisotropic orbital depairing (AOD) effect due to the layered crystal structure, and

the enhanced magnetic permeability (EMP) effect resulting from the anisotropy of the $Nd^{3+}4f$ magnetic moment (Figs. 13(i)-13(j)), which is unique to Nd-nickelate [69]. The AOD effect accounts for the θ dependence of magnetoresistance observed in La- and Pr-nickelate, exhibiting a minimum resistance with in-plane magnetic fields. Regarding the EMP effect, the magnetic susceptibility of Nd^{3+} exhibits a clover-leaf pattern, leading to maximum amplification of the local in-plane magnetic field, thereby enhancing the depairing effect and suppressing superconductivity. The investigation into the magnetoresistance of infinite-layer nickelate $Nd_{0.8}Sr_{0.2}NiO_2$ superconducting films [68] not only revealed an azimuthal clover-leaf pattern but also identified an additional two-fold (C_2) symmetric component in the $R(\phi)$ curves as the system approached low temperatures and high magnetic fields.

5.2. Anisotropy of H_{c2} in infinite-layer nickelate superconductors

Harold Y. Hwang discovered that H_{c2} is surprisingly isotropic at low temperatures in $Nd_{0.775}Sr_{0.225}NiO_2$ thin

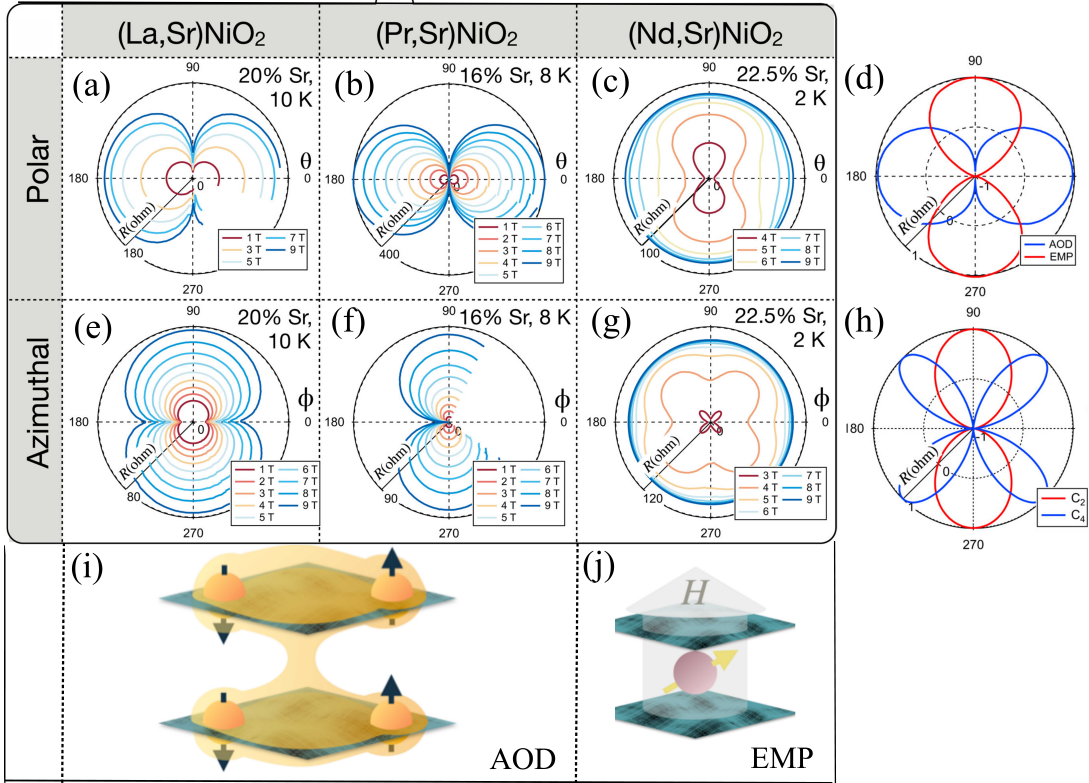


FIG. 13. Polar (a-c) and azimuthal (e-g) angle dependence of magnetoresistance in the superconducting transition region for La-, Pr-, and Nd-nickelates. (d and h) Fitting functions representing the AOD and EMP effects for θ - and ϕ -dependence. Schematic representations of (i) anisotropic orbital depairing (AOD) and (j) enhanced magnetic permeability (EMP) [69].

films with T_c of 8.5 K, despite the layered crystal structure, quasi-2D band structure ($d_{x^2-y^2}$) and the thin film geometry (as shown in Fig. 11(a)) [25]. Interestingly, the observed isotropy in $\text{Nd}_{0.775}\text{Sr}_{0.225}\text{NiO}_2$ differs from the anisotropic $H_{c2}(T)$ behavior observed in infinite-layer nickelate superconductors, such as the high-quality $\text{La}_{0.8}\text{Sr}_{0.2}\text{NiO}_2$ thin film. In Fig. 14(c), the H_{c2} anisotropy ($\gamma = H_{c2}^{ab}/H_{c2}^c$) decreased monotonically from ~ 10 near T_c to ~ 1.5 at 2 K in a high-quality $\text{La}_{0.8}\text{Sr}_{0.2}\text{NiO}_2$ thin film with $T_c^{\text{onset}} = 18.8$ K. The γ value in high-quality thin film is somewhat larger compared to previous reports on lower-quality thin films with lower T_c (7 for $\text{La}_{0.8}\text{Sr}_{0.2}\text{NiO}_2$ and 6 for $\text{La}_{0.8}\text{Ca}_{0.2}\text{NiO}_2$ near T_c) [69]. For $\text{Nd}_{0.775}\text{Sr}_{0.225}\text{NiO}_2$, the isotropy can be attributed to the easy-plane magnetic anisotropy of the Nd^{3+} $4f$ moment, which increases the in-plane magnetic susceptibility, enhancing the suppression of superconductivity. First-principles calculations reveal that in LaNiO_2 , two small electron-like pockets around the Γ and A points are mainly derived from La orbitals, and with approximately 20% hole doping, only a reduced 3D electron pocket remains at the A point. Therefore, the anisotropy seen in $\text{La}_{0.8}\text{Sr}_{0.2}\text{NiO}_2$ thin films may be intrinsic to infinite-layer nickelates, unaffected by Nd^{3+} magnetism, while orbital hybridization at lower

temperatures increases electron coupling, thus reducing anisotropy.

Angular dependence of H_{c2} can also provide valuable information about a superconductor's depairing processes and dimensionality. As shown in Fig. 14(a), although angular modulation is clearly present in $\text{Nd}_{0.775}\text{Sr}_{0.225}\text{NiO}_2$, the magnitude of H_{c2} remains predominantly isotropic and becomes more pronounced at lower temperatures [25]. Figs. 14(d-f) present the angle dependence of the normalized H_{c2} at 2 K, 4.2 K, and 10 K for a high-quality $\text{La}_{0.8}\text{Sr}_{0.2}\text{NiO}_2$ thin film [30]. By fitting the data using both the 3D GL model and the 2D Tinkham model, a dimensional crossover from 2D to 3D superconductivity with decreasing temperature is observed. Such a crossover may be attributed to the hybridization of rare-earth $5d$ and Ni $3d$ orbitals, forming interstitial- s orbital, which enhances the coupling strength between the NiO_2 planes and the rare-earth spacer layers at lower temperatures [84, 85]. However, all infinite-layer nickel-based 112 thin films studied thus far remain in the dirty limit, and further improvements in sample quality could help clarify the issue of H_{c2} anisotropy.

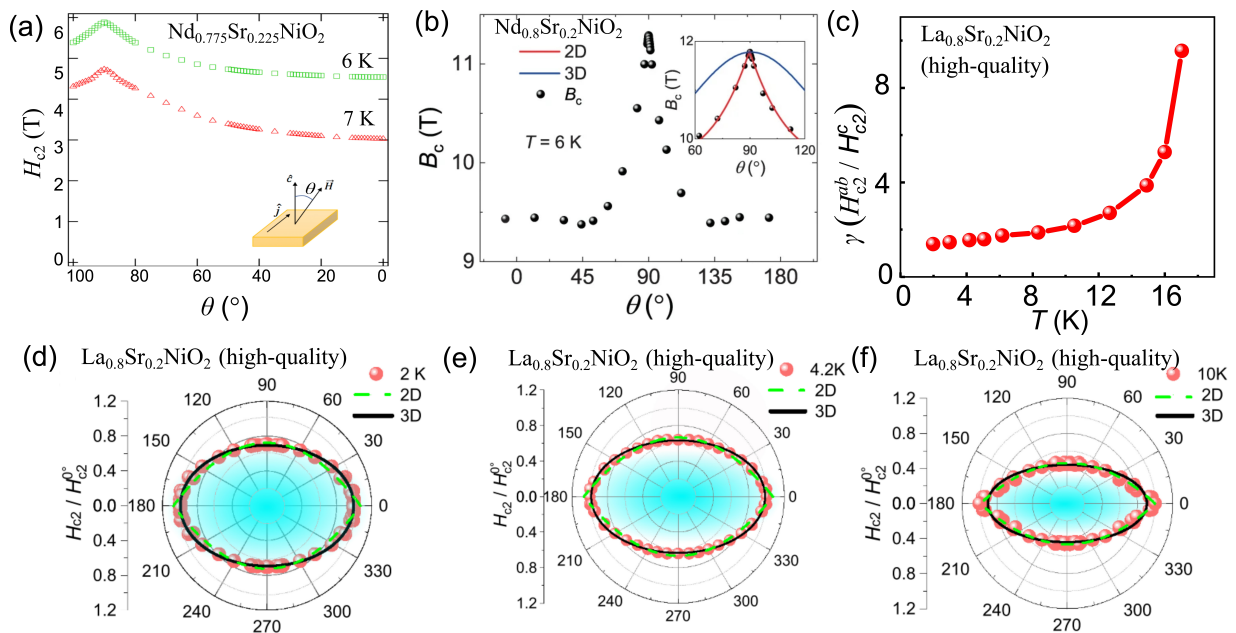


FIG. 14. (a-b) Polar angle dependence of H_{c2} in $\text{Nd}_{0.775}\text{Sr}_{0.225}\text{NiO}_2$ and $\text{Nd}_{0.8}\text{Sr}_{0.2}\text{NiO}_2$ [25, 68]. Inset of (a) shows a schematic definition of the magnetic field orientation angle θ . (c) Anisotropy of H_{c2} ($\gamma = H_{c2}^{ab}/H_{c2}^c$) for the high-quality $\text{La}_{0.8}\text{Sr}_{0.2}\text{NiO}_2$ thin film [30]. (d-e) Polar angle dependence of the normalized $H_{c2}(\theta)/H_{c2}^0$, for the high-quality $\text{La}_{0.8}\text{Sr}_{0.2}\text{NiO}_2$ thin film at various temperatures [30].

6. Conclusions and outlook

The study of H_{c2} is crucial to the mechanism of the superconducting pair-breaking mechanism and the symmetry of superconducting pairing, which is mainly reflected in the following aspects:

(i) The study of the temperature dependence of $H_{c2}(T)$ is crucial for understanding the fundamental physics of superconductivity, as it provides insights into the pairing mechanisms and limiting factors that govern superconducting behavior. Near T_c , the orbital depairing effect, which arises from the Lorentz force acting on Cooper pairs in the presence of a magnetic field, is the dominant factor limiting H_{c2} . In contrast, at low temperatures and under high magnetic fields, the spin-paramagnetic depairing effect becomes the primary constraint, where the Zeeman energy disrupts the Cooper pairs. Furthermore, unconventional superconducting states, such as the spin-triplet p -wave pairing state [86], the non-zero momentum FFLO state most in FeSCs [87–89], the strongly correlated Bose-Einstein - Condensation (BEC) superconducting state [90], and multi-band superconducting states [17], can significantly affect the temperature dependence of H_{c2} , even leading to the appearance of high-field phases in the low-temperature region [79, 91, 92].

(ii) Anisotropy of H_{c2} . As a fundamental parameter, the superconducting anisotropy $r = H_{c2}^{ab}/H_{c2}^c$ plays a key role in understanding the superconducting mechanism and its potential applications. The anisotropy of

H_{c2} directly reflects the dimensionality of superconductivity. The in-plane anisotropy of H_{c2} is closely related to the structure of the superconducting gap and pairing symmetry. For instance, in cuprate superconductors, the in-plane H_{c2} shows fourfold symmetry (d -wave) [93], and in nickelate superconductors, there is mixed symmetry (possibly $s + d$ -wave) [68]. Additionally, when the superconducting state is influenced by factors such as charge order, nematic phases, or strong spin-orbit coupling, as seen in FeSCs, changes in the symmetry of the superconducting wave function can also be reflected in the angular dependence of H_{c2} .

(iii) Doping dependence of H_{c2} . The variation of H_{c2} with doping concentration can be used to track changes in the strength of the pairing potential, where higher H_{c2} corresponds to the stronger pairing potential and a smaller pairing size. On the other hand, the variation of H_{c2} with doping or pressure can directly reflect the relationship between superconductivity and other electronic ordered states, helping to precisely determine the location of the quantum critical point (QCP) and providing clues for understanding the superconducting pairing mechanism.

The analysis of across these superconductors deepens our understanding of the superconducting pairing mechanisms and pairing symmetry, providing valuable directions for future research.

Acknowledgements

This work was partly supported by the National Natural Science Foundation of China (Grants No. 12374135, No. 12374136, No. U1932217, No. 12204487), and the Natural Science Foundation of Shandong Province (No. ZR2022QA040, No. ZR2023QA057).

W.W and Y.X. contributed equally to this work.

W.W. and Y.X. designed and wrote the manuscript with the help of Q.H., Y.S. and Z.S. All authors have read and agreed to the published version of the manuscript.

Conflicts of Interest: The authors declare no conflict of interest.

* Corresponding author: sunyue@seu.edu.cn

† Corresponding author: zxsshi@seu.edu.cn

- [1] Bednorz J G and Müller K A 1986 Possible high-Tc superconductivity in the Ba-La-Cu-O system. *Z. Phys. B Condens. Matter* **64** 189–193
- [2] Kamihara Y, Hiramatsu H, Hirano M, Kawamura R, Yanagi H, Kamiya T and Hosono H 2006 Iron-based layered superconductor: LaOFeP. *J. Am. Chem. Soc.* **128** 10012–10013
- [3] Kamihara Y, Watanabe T, Hirano M and Hosono H 2008 Iron-based layered superconductor La[O_{1-x}F_x]FeAs ($x = 0.05 - 0.12$) with $T_c = 26$ K. *J. Am. Chem. Soc.* **130** 3296–3297
- [4] Li D, Lee K, Wang B Y, Osada M, Crossley S, Lee H R, Cui Y, Hikita Y and Hwang H Y 2019 Superconductivity in an infinite-layer nickelate. *Nature* **572** 624–627
- [5] Sun H, Huo M, Hu X, Li J, Liu Z, Han Y, Tang L, Mao Z, Yang P, Wang B et al 2023 Signatures of superconductivity near 80 K in a nickelate under high pressure. *Nature* **621** 493–498
- [6] Hunte F, Jaroszynski J, Gurevich A, Larbalestier D C, Jin R, Sefat A S, McGuire M A, Sales B C, Christen D K and Mandrus D 2008 Two-band superconductivity in LaFeAsO_{0.89}F_{0.11} at very high magnetic fields. *Nature* **453** 903–905
- [7] Zhuang J C, Li Z, Xu X, Wang L, Yeoh W K, Xing X Z, Shi Z X, Wang X L, Du Y and Dou S X 2015 Pauli-limited effect in the magnetic phase diagram of FeSe_xTe_{1-x} thin films. *Appl. Phys. Lett.* **107** 22
- [8] Xing X Z, Zhou W, Wang J H, Zhu Z, Zhang Y F, Zhou N, Qian B, Xu X F and Shi Z X 2017 Two-band and Pauli-limiting effects on the upper critical field of 112-type iron pnictide superconductors. *Sci. Rep.* **7** 45943
- [9] Keimer B, Kivelson S A, Norman M R, Uchida S and Zaanen J 2015 From quantum matter to high-temperature superconductivity in copper oxides. *Nature* **518** 179–186
- [10] Goodge B H, Li D, Lee K, Osada M, Wang B Y, Sawatzky G A, Hwang H Y and Kourkoutis L F 2021 Doping evolution of the Mott-Hubbard landscape in infinite-layer nickelates. *Proc. Natl. Acad. Sci. USA* **118** e2007683118
- [11] Ren Z A and Zhao Z X 2009 Research and prospects of iron-based superconductors. *Adv. Mater.* **21** 4584–4592
- [12] Hepting M, Li D, Jia C J, Lu H, Paris E, Tseng Y, Feng X, Osada M, Been E, Hikita Y et al 2020 Electronic structure of the parent compound of superconducting infinite-layer nickelates. *Nat. Mater.* **19** 381–385
- [13] Hu J 2016 Identifying the genes of unconventional high temperature superconductors. *Sci. Bull.* **61** 561–569
- [14] Damascelli A, Hussain Z and Shen Z-X 2003 Angle-resolved photoemission studies of the cuprate superconductors. *Rev. Mod. Phys.* **75** 473
- [15] Llovo I F, Carballeira C, Soñora D, Pereiro A, Ponte J J, Salem-Sugui S Jr, Sefat A S and Mosqueira J 2021 Multiband effects on the upper critical field angular dependence of 122-family iron pnictide superconductors. *Sci. Rep.* **11** 11526
- [16] Li D, Wang B Y, Lee K, Harvey S P, Osada M, Goodge B H, Kourkoutis L F and Hwang H Y 2020 Superconducting dome in Nd_{1-x}Sr_xNiO₂ infinite layer films. *Phys. Rev. Lett.* **125** 027001
- [17] Gurevich A 2003 Enhancement of the upper critical field by nonmagnetic impurities in dirty two-gap superconductors. *Phys. Rev. B* **67** 184515
- [18] Golubov A A, Kortus J, Dolgov O V, Jepsen O, Kong Y, Andersen O K, Gibson B J, Ahn K and Kremer R K 2002 Specific heat of MgB₂ in a one- and a two-band model from first-principles calculations. *J. Phys. Condens. Matter* **14** 1353
- [19] Bristow M 2020 Iron-based superconductors in high magnetic fields. *Christ Church College, University of Oxford*
- [20] Werthamer N R, Helfand E and Hohenberg P C 1966 Temperature and purity dependence of the superconducting critical field, H_{c2} . III. Electron spin and spin-orbit effects. *Phys. Rev.* **147** 295–302
- [21] Clogston A M 1962 Upper limit for the critical field in hard superconductors. *Phys. Rev. Lett.* **9** 266
- [22] Chandrasekhar B S 1962 A note on the maximum critical field of high-field superconductors. *Appl. Phys. Lett.* **1**
- [23] Charikova T B, Shelushinina N G, Harus G I, Petukhov D S, Neverov V N and Ivanov A A 2013 Upper critical field in electron-doped cuprate superconductor Nd_{2-x}Ce_xCuO₄ + δ : Two-gap model. *Physica C: Superconductivity* **488** 25–29
- [24] Li Y, Tabis W, Tang Y, Yu G, Jaroszynski J, Barišić N and Greven M 2019 Hole pocket-driven superconductivity and its universal features in the electron-doped cuprates. *Science Advances* **5** eaap7349
- [25] Wang B Y, Li D, Goodge B H, Lee K, Osada M, Harvey S P, Kourkoutis L F, Beasley M R and Hwang H Y 2021 Isotropic Pauli-limited superconductivity in the infinite-layer nickelate Nd_{0.775}Sr_{0.225}NiO₂. *Nature Physics* **17** 473–477
- [26] Gurevich A 2007 Limits of the upper critical field in dirty two-gap superconductors. *Physica C: Superconductivity* **456** 160–169
- [27] Gurevich A 2010 Upper critical field and the Fulde-Ferrel-Larkin-Ovchinnikov transition in multiband superconductors. *Phys. Rev. B—Condensed Matter and Materials Physics* **82** 184504
- [28] Gorkov L P 1984 Anisotropy of the upper critical field in exotic superconductors. *JETP Letters* **40** 1155–1158
- [29] Blatter G, Geshkenbein V B and Larkin A I 1992 From isotropic to anisotropic superconductors: A scaling approach. *Phys. Rev. Lett.* **68** 875
- [30] Wei W, Sun W, Sun Y, Pan Y Q, Jin G J, Yang F, Li Y Y, Zhu Z W, Nie Y F and Shi Z X 2023 Large upper critical fields and dimensionality crossover of superconductivity in the infinite-layer nickelate La_{0.8}Sr_{0.2}NiO₂. *Phys. Rev.*

B 107 L220503

- [31] Monteiro A M R V L, Groenendijk D J, Groen I, de Bruijkere J, Gaudenzi R, Van Der Zant H S J and Caviglia A D 2017 Two-dimensional superconductivity at the (111) $\text{LaAlO}_3/\text{SrTiO}_3$ interface. *Phys. Rev. B* **96** 020504
- [32] Sekitani T, Miura N, Ikeda S, Matsuda Y H and Shiohara Y 2004 Upper critical field for optimally-doped $\text{YBa}_2\text{Cu}_3\text{O}_{7-\delta}$. *Physica B: Condensed Matter* **346** 319–324
- [33] Jovanović V P, Li Z Z, Raffy H, Briatico J, Sinchenko A A and Monceau P 2009 Resistive upper critical fields and anisotropy of an electron-doped infinite-layer cuprate. *Phys. Rev. B—Condensed Matter and Materials Physics* **80** 024501
- [34] Wu G, Greene R L, Reyes A P, Kuhns P L, Moulton W G, Wu B, Wu F and Clark W G 2014 Superconducting anisotropy in the electron-doped high- T_c superconductors $\text{Pr}_{2-x}\text{Ce}_x\text{CuO}_{4-y}$. *J. Phys.: Condensed Matter* **26** 405701
- [35] Gantmakher V F, Emel'chenko G A, Naumenko I G and Tsydynzhapov G E 2000 Temperature dependence of the upper critical field as an indicator of boson effects in superconductivity in $\text{Nd}_{2-x}\text{Ce}_x\text{CuO}_{4-y}$. *J. Exp. Theor. Phys. Lett.* **72** 21–25
- [36] Vedenev S I, Proust C, Mineev V P, Nardone M and Rikken G L J A 2006 Reaching the Pauli limit in the cuprate $\text{Bi}_2\text{Sr}_2\text{CuO}_{6+\delta}$ in high parallel magnetic fields. *Phys. Rev. B—Condensed Matter and Materials Physics* **73** 014528
- [37] Gollnik F and Naito M 1998 Doping dependence of normal- and superconducting-state transport properties of $\text{Nd}_{2-x}\text{Ce}_x\text{CuO}_{4+y}$ thin films. *Phys. Rev. B* **58** 11734
- [38] Charikova T B, Shelushinina N G, Kharus G I and Ivanov A A 2008 Effect of the nonstoichiometric disorder on the temperature dependence of the upper critical field in $\text{Nd}_{2-x}\text{Ce}_x\text{CuO}_{4+\delta}$ electron superconductors. *JETP Lett.* **88** 123–126
- [39] Vedenev S I, Maude D K, Haanappel E and Mineev V P 2007 C-axis resistivity of La-free $\text{Bi}_{2+x}\text{Sr}_{2-x}\text{CuO}_{6+\delta}$ single crystals in high magnetic fields. *Phys. Rev. B—Condensed Matter and Materials Physics* **75** 064512
- [40] Teng M L, Yin Y W, Xie L and Li X G 2013 Stripe order related in-plane fourfold symmetric superconductivity in $\text{La}_{1.45}\text{Nd}_{0.4}\text{Sr}_{0.15}\text{CuO}_4$ single crystal. *J. Appl. Phys.* **113** 5
- [41] Grissonnanche G, Cyr-Choinière O, Laliberté F S, René de Cotret S, Juneau-Fecteau A, Dufour-Beauséjour S, Delage M-E, LeBoeuf D, Chang J, Ramshaw B J et al 2014 Direct measurement of the upper critical field in cuprate superconductors. *Nature Communications* **5** 3280
- [42] Wang Y, Li L and Ong N P 2006 Nernst effect in high- T_c superconductors. *Phys. Rev. B—Condensed Matter and Materials Physics* **73** 024510
- [43] Wang Y, Ono S, Onose Y, Gu G, Ando Y, Tokura Y, Uchida S and Ong N P 2003 Dependence of upper critical field and pairing strength on doping in cuprates. *Science* **299** 86–89
- [44] Tallon J L and Loram J W 2001 The doping dependence of T^* —what is the real high- T_c phase diagram? *Physica C: Superconductivity* **349** 53–68
- [45] LeBoeuf D, Doiron-Leyraud N, Vignolle B, Sutherland M, Ramshaw B J, Levallois J, Daou R, Laliberté F, Cyr-Choinière O, Chang J et al 2011 Lifshitz critical point in the cuprate superconductor $\text{YBa}_2\text{Cu}_3\text{O}_y$ from high-field Hall effect measurements. *Phys. Rev. B—Condensed Matter and Materials Physics* **83** 054506
- [46] Bonn D A, Kamal S, Bonakdarpour A, Liang R, Hardy W N, Homes C C, Basov D N and Timusk T 1996 Surface impedance studies of YBCO. *Czechoslovak J. Phys.* **46** 3195–3202
- [47] Uemura Y J, Luke G M, Sternlieb B J, Brewer J H, Carolan J F, Hardy W N, Kadono R, Kempton J R, Kiefl R F, Kreitzman S R et al 1989 Universal correlations between T_c and $n_s m^*$ (carrier density over effective mass) in high- T_c cuprate superconductors. *Phys. Rev. Lett.* **62** 2317
- [48] Zhou N, Sun Y, Xi C Y, Wang Z S, Zhang J L, Zhang Y, Zhang Y F, Xu C Q, Pan Y Q, Feng J J et al 2021 Disorder-robust high-field superconducting phase of FeSe single crystals. *Phys. Rev. B* **104** L140504
- [49] Pan Y Q, Sun Y, Zhou N, Yi X L, Hou Q, Wang J H, Zhu Z W, Mitamura H, Tokunaga M and Shi Z X 2024 Novel anisotropy of upper critical fields in $\text{Fe}_{1+y}\text{Te}_{0.6}\text{Se}_{0.4}$. *J. Alloys Compd.* **976** 173262
- [50] Zhang J L, Jiao L, Balakirev F F, Wang X C, Jin C Q and Yuan H Q 2011 Upper critical field and its anisotropy in LiFeAs . *Phys. Rev. B—Condensed Matter and Materials Physics* **83** 174506
- [51] Cho C W, Yang J H, Yuan N F Q, Shen J Y, Wolf T and Lortz R 2017 Thermodynamic evidence for the Fulde-Ferrell-Larkin-Ovchinnikov state in the KFe_2As_2 superconductor. *Phys. Rev. Lett.* **119** 217002
- [52] Terashima T, Kimata M, Satsukawa H, Harada A, Hazama K, Uji S, Harima H, Chen G-F, Luo J-L and Wang N-L 2009 Resistivity and upper critical field in KFe_2As_2 single crystals. *J. Phys. Soc. Japan* **78** 063702–063702
- [53] Yuan H Q, Singleton J, Balakirev F F, Baily S A, Chen G-F, Luo J L and Wang N L 2009 Nearly isotropic superconductivity in $(\text{Ba,K})\text{Fe}_2\text{As}_2$. *Nature* **457** 565–568
- [54] Ding H, Richard P, Nakayama K, Sugawara K, Arakane T, Sekiba Y, Takayama A, Souma S, Sato T and Takahashi T 2008 Observation of Fermi-surface-dependent nodeless superconducting gaps in $\text{Ba}_{0.6}\text{K}_{0.4}\text{Fe}_2\text{As}_2$. *Europhys. Lett.* **83** 47001
- [55] Matsuda Y and Shimahara H 2007 Fulde-Ferrell-Larkin-Ovchinnikov state in heavy fermion superconductors. *J. Phys. Soc. Japan* **76** 051005
- [56] Takada S 1970 Superconductivity in a molecular field. II: Stability of Fulde-Ferrell phase. *Prog. Theor. Phys.* **43** 27–38
- [57] Cui Q and Yang K 2008 Fulde-Ferrell-Larkin-Ovchinnikov state in disordered s-wave superconductors. *Phys. Rev. B—Condensed Matter and Materials Physics* **78** 054501
- [58] Vorontsov A B, Sauls J A and Graf M J 2005 Phase diagram and spectroscopy of Fulde-Ferrell-Larkin-Ovchinnikov states of two-dimensional d-wave superconductors. *Phys. Rev. B—Condensed Matter and Materials Physics* **72** 184501
- [59] Ptok A 2010 The Fulde-Ferrell-Larkin-Ovchinnikov superconductivity in disordered systems. *Acta Physica Polonica A* **118** (2)
- [60] Borg C K H, Zhou X, Eckberg C, Campbell D J, Saha S R, Paglione J and Rodriguez E E 2016 Strong anisotropy in nearly ideal tetrahedral superconducting FeS single crystals. *Phys. Rev. B* **93** 094522

- [61] Zhou W, Xing X, Zhao H, Feng J, Pan Y Q, Zhou N, Zhang Y F, Qian B and Shi Z X 2017 Anomalous electron doping independent two-dimensional superconductivity. *New J. Phys.* **19** 073014
- [62] Li J, Pereira P J, Yuan J, Lv Y-Y, Jiang M-P, Lu D, Lin Z-Q, Liu Y-J, Wang J-F, Li L et al 2017 Nematic superconducting state in iron pnictide superconductors. *Nat. Commun.* **8** 1880
- [63] Liang Q, Liu T, Xi C, Han Y, Mu G, Pi L, Ren Z-A, and Wang Z-S 2019 Upper critical field and its anisotropy in RbCr_3As_3 . *Phys. Rev. B* **100** (21) 214512
- [64] Balakirev F F, Kong T, Jaime M, McDonald R D, Mielke C H, Gurevich A, Canfield P C, and Bud'ko S L 2015 Anisotropy reversal of the upper critical field at low temperatures and spin-locked superconductivity in $\text{K}_2\text{Cr}_3\text{As}_3$. *Phys. Rev. B* **91** (22) 220505
- [65] Cao G-H and Zhu Z-W 2018 Superconductivity with peculiar upper critical fields in quasi-one-dimensional Cr-based pnictides. *Chin. Phys. B* **27** (10) 107401
- [66] Mukasa K, Ishida K, Imajo S, Qiu M, Saito M, Matsuura K, Sugimura Y, Liu S, Uezono Y, Otsuka T, et al. 2023 Enhanced superconducting pairing strength near a pure nematic quantum critical point. *Phys. Rev. X* **13** (1) 011032
- [67] Ishida K, Onishi Y, Tsujii M, Mukasa K, Qiu M, Saito M, Sugimura Y, Matsuura K, Mizukami Y, Hashimoto K, et al. 2022 Pure nematic quantum critical point accompanied by a superconducting dome. *Proc. Natl. Acad. Sci.* **119** (18) e2110501119
- [68] Ji H, Liu Y, Li Y, Ding X, Xie Z-Y, Ji C-C, Qi S-C, Gao X-Y, Xu M-H, Gao P, et al. 2023 Rotational symmetry breaking in superconducting nickelate $\text{Nd}_{0.8}\text{Sr}_{0.2}\text{NiO}_2$ films. *Nat. Commun.* **14** (1) 7155
- [69] Wang B Y, Wang T C, Hsu Y-T, Osada M, Lee K, Jia C, Duffy C, Li D, Fowlie J, Beasley M R, et al. 2023 Effects of rare-earth magnetism on the superconducting upper critical field in infinite-layer nickelates. *Sci. Adv.* **9** (20) eadf6655
- [70] Fang M, Yang J, Balakirev F F, Kohama Y, Singleton J, Qian B, Mao Z Q, Wang H, and Yuan H Q 2010 Weak anisotropy of the superconducting upper critical field in $\text{Fe}_{1.11}\text{Te}_{0.6}\text{Se}_{0.4}$ single crystals. *Phys. Rev. B* **81** (2) 020509
- [71] Khim S, Kim J W, Choi E S, Bang Y, Nohara M, Takagi H, and Kim K H 2010 Evidence for dominant Pauli paramagnetic effect in the upper critical field of single-crystalline $\text{FeTe}_{0.6}\text{Se}_{0.4}$. *Phys. Rev. B* **81** (18) 184511
- [72] Harper F E and Tinkham M 1968 The mixed state in superconducting thin films. *Phys. Rev.* **172** (2) 441
- [73] Abrikosov A A and Gor'kov L P 1960 Contribution to the theory of superconducting alloys with paramagnetic impurities. *Zhur. Eksptl'. i Teoret. Fiz.* **39**
- [74] Tinkham M 2004 *Introduction to Superconductivity*, volume 1. Courier Corporation
- [75] Maloney M D, Cruz F de la, and Cardona M 1972 Superconducting parameters and size effects of aluminum films and foils. *Phys. Rev. B* **5** (9) 3558
- [76] Hsu Y-T, Wang B Y, Berben M, Li D, Lee K, Duffy C, Ottenbros T, Kim W J, Osada M, Wiedmann S, et al. 2021 Insulator-to-metal crossover near the edge of the superconducting dome in $\text{Nd}_{1-x}\text{Sr}_x\text{NiO}_2$. *Phys. Rev. Res.* **3** (4) L042015
- [77] Kitagawa S, Nakamine G, Ishida K, Jeevan H S, Geibel C, and Steglich F 2018 Evidence for the presence of the Fulde-Ferrell-Larkin-Ovchinnikov state in CeCu_2Si_2 revealed using ^{63}Cu NMR. *Phys. Rev. Lett.* **121** (15) 157004
- [78] Singleton J, Symington J A, Nam M S, Arda van A, Kurmoo M, and Day P 2000 Observation of the Fulde-Ferrell-Larkin-Ovchinnikov state in the quasi-two-dimensional organic superconductor κ -(BEDT-TTF) $_2\text{Cu}$ (NCS) $_2$ (BEDT-TTF = bis(ethylene-dithio)tetrathiafulvalene). *J. Phys.: Condens. Matter* **12** (40) L641
- [79] Kenzelmann M, Strassle T, Niedermayer Ch, Sigrist M, Padmanabhan B, Zolliker M, Bianchi A D, Movshovich R, Bauer E D, Sarrao J L, et al. 2008 Coupled superconducting and magnetic order in CeCoIn_5 . *Science* **321** (5896) 1652–1654
- [80] Kenzelmann M, Gerber S, Egetenmeyer N, Gavilano J L, Strässle T, Bianchi A D, Ressouche E, Movshovich R, Bauer E D, Sarrao J L, et al. 2010 Evidence for a magnetically driven superconducting Q -phase of CeCoIn_5 . *Phys. Rev. Lett.* **104** (12) 127001
- [81] Ihara H, Iyo A, Tanaka K, Tokiwa K, Ishida K, Terada N, Tokumoto M, Sekita Y, Tsukamoto T, Watanabe T, et al. 1997 How to make superconducting anisotropy least in high- T_c cuprate superconductors. *Physica C: Superconductivity and its applications* **282** 1973–1974
- [82] Iye Y, Fukushima A, Tamegai T, Terashima T, and Bando Y 1991 Anisotropy and dissipation in the mixed state of high temperature superconductors. *Physica C: Superconductivity* **185** 297–302
- [83] Iye Y, Watanabe A, Nakamura S, Tamegai T, Terashima T, Yamamoto K, and Bando Y 1990 Dissipation in the mixed state of conventional and high temperature superconductors. *Physica C: Superconductivity* **167** (3-4) 278–286
- [84] Wang Z, Zhang G-M, Yang Y-F, and Zhang F-C 2020 Distinct pairing symmetries of superconductivity in infinite-layer nickelates. *Phys. Rev. B* **102** (22) 220501
- [85] Gu Y, Zhu S, Wang X, Hu J and Chen H 2020 A substantial hybridization between correlated Ni- d orbital and itinerant electrons in infinite-layer nickelates. *Commun. Phys.* **3** 84.
- [86] Bay T V, Naka T, Huang Y K, Luigjes H, Golden M S, and De Visser A 2012 Superconductivity in the doped topological insulator $\text{Cu}_x\text{Bi}_2\text{Se}_3$ under high pressure. *Phys. Rev. Lett.* **108** (5) 057001
- [87] Fulde P and Ferrell R A 1964 Superconductivity in a strong spin-exchange field. *Phys. Rev.* **135** (3A) A550
- [88] Larkin A I and Ovchinnikov Y N 1965 Nonuniform state of superconductors. *Sov. Phys. JETP* **20** (3) 762–762
- [89] Kasahara S, Sato Y, Licciardello S, Čulo M, Arsenijević S, Ottenbros T, Tominaga T, Böker J, Eremin I, Shibauchi T, et al. 2020 Evidence for a Fulde-Ferrell-Larkin-Ovchinnikov state with segmented vortices in the BCS-BEC-crossover superconductor FeSe . *Phys. Rev. Lett.* **124** (10) 107001
- [90] Kuchinskii E Z, Kuleeva N A, and Sadovskii M V 2017 Temperature dependence of the upper critical field in disordered Hubbard model with attraction. *J. Exp. Theor. Phys.* **125** 1127–1136
- [91] Beyer R, Bergk B, Yasin S, Schlueter J A, and Wosnitza J 2012 Angle-dependent evolution of the Fulde-Ferrell-Larkin-Ovchinnikov state in an organic superconductor. *Phys. Rev. Lett.* **109** (2) 027003
- [92] Kasahara S, Watashige T, Hanaguri T, Kohsaka Y, Ya-

- mashita T, Shimoyama Y, Mizukami Y, Endo R, Ikeda H, Aoyama K, et al. 2014 Field-induced superconducting phase of FeSe in the BCS-BEC cross-over. *Proc. Natl. Acad. Sci. USA* **111** (46) 16309–16313
- [93] Koike Y, Takabayashi T, Noji T, Nishizaki T, and Kobayashi N 1996 Fourfold symmetry in the ab -plane of the upper critical field for single-crystal $\text{Pb}_2\text{Sr}_2\text{Y}_{0.62}\text{Ca}_{0.38}\text{Cu}_3\text{O}_8$: Evidence for $d_{x^2-y^2}$ pairing in a high- T_c superconductor. *Phys. Rev. B* **54** (2) R776